Charles University in Prague
Faculty of Mathematics and Physics

BACHELOR THESIS

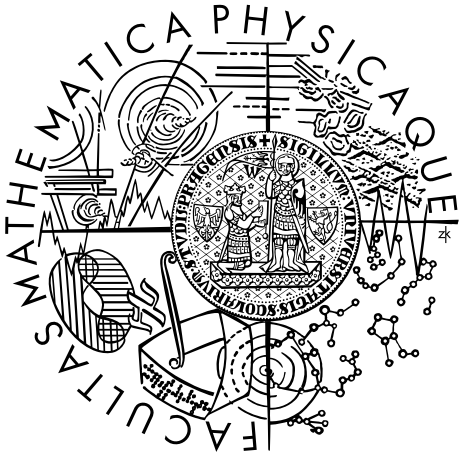

Lýdia Štofanová

Coherent dusty and gaseous structures near the Galactic centre

Astronomical Institute of the Charles University

Supervisor of the bachelor thesis:	Prof. RNDr. Vladimír Karas, DrSc.
Consultee of the bachelor thesis:	RNDr. Michal Zajaček
Study programme:	Physics
Study branch:	General Physics

Prague 2016

I declare that I carried out this bachelor thesis independently, and only with the cited sources, literature and other professional sources.

I understand that my work relates to the rights and obligations under the Act No. 121/2000 Sb., the Copyright Act, as amended, in particular the fact that the Charles University in Prague has the right to conclude a license agreement on the use of this work as a school work pursuant to Section 60 subsection 1 of the Copyright Act.

In Prague, 24 May 2016 Lýdia Štofanová

Dedication. I would like to thank my supervisor Prof. Vladimír Karas who responsibly supervised this thesis. Although, he has a very busy schedule as the director of the Astronomical Institute, Academy of Sciences of the Czech Republic, he has always found time to discuss variety of problems which arose during our collaboration and he was always willing to explain issues that were hard for me to understand. I really appreciate his help. I would like to thank him also for giving me a chance to paticipate in the ESO/Opticon/IAU summer school, which took place in Brno in September 2015, and which was primarily meant for advanced MSc students and more senior astronomers. I have gained a lot of experience, learned many new things and got to know the community of astronomers as well. Especially, I would like to thank Dr. Petr Kabáth for the organization of this helpful summer school.

I am grateful for the support and long discussions with my consultee RNDr. Michal Zajaček. Despite the fact that the most of the time he spends in Germany, he has been available to help me whenever I needed. Not only did he always answer my never-ending avalanche of questions but he also had great advice and interesting ideas how to improve this bachelor thesis.

I would like to thank both my supervisor and my consultee for the opportunity to attend CPP15 – Cologne-Prague Meeting in Prague 2015: From supermassive black holes to star formation in Galactic nuclei – that they successfully organized. This event was specialized in the Galactic centre that is the main region of our interest in this bachelor thesis. It was very fruitful experience because the presentations of individual participants covered various topics from the closest region around the central supermassive black hole and on the top of that these presentations included the newest results and research made by these participants. It was also my pleasure to meet with Prof. Andreas Eckart and the whole group of his students and collaborators.

Last but not least, I am beyond grateful for all the support from my loving parents during my studies at the Charles University in Prague.

Title: Coherent dusty and gaseous structures near the Galactic centre

Author: Lýdia Štofanová

Department: Astronomical Institute of the Charles University in Prague

Supervisor: Prof. RNDr. Vladimír Karas, DrSc., Astronomical Institute of the Academy of Sciences of the Czech Republic

Consultee: RNDr. Michal Zajaček, I. Physikalisches Institut Universität zu Köln, Max Planck Institut für Radioastronomie and Astronomical Institute of the Academy of Sciences of the Czech Republic

Abstract: Sagittarius A*, a compact source in the centre of the Milky Way, is the nearest supermassive black hole (SMBH) in our cosmic neighbourhood, where various astrophysical processes take place. In consequence, variety of structures emerge near the Galactic centre and bow shocks that are closely studied in this work represent an example of them. The introductory part of this thesis is a brief review of the history of the Galactic centre research and its discovery in radio wavelengths. The main body of the thesis is focused on a simplified model of the bow-shock structures that are generated by stars moving supersonically with respect to the ambient medium. We discuss how these structures vary along the orbit. To this end, we consider four different models: (a) without the presence of any gaseous medium emerging from or accreting onto the SMBH, (b) taking an outflow from the SMBH into account, (c) the case of an inflow onto the SMBH, and finally (d) the combined model involving both an outflow and an inflow at the same time. We discuss symmetries of each model (or lack of them) and we find that the model considering the ambient medium at rest appears symmetrical with respect to the pericentre passage. The combined model manifests itself as the most asymmetrical one of them all. We show profiles for the tangential velocity in the shell and the mass surface density of the bow-shock shell along the stellar orbit for all considered models.

Keywords: Galactic centre; Astrophysical processes; Bow shocks; Interstellar medium

Název práce: Koherentní pracho-plynné struktury v blízkém okolí jádra Galaxie

Autor: Lýdia Štofanová

Katedra: Astronomický ústav Univerzity Karlovy v Praze

Vedoucí práce: Prof. RNDr. Vladimír Karas, DrSc., Astronomický ústav Akademie věd České republiky

Konzultant: RNDr. Michal Zajaček, 1. Fyzikální ústav Univerzity v Kolíne nad Rýnem, Ústav Maxa Plancka pro Radioastronomii a Astronomický ústav Akademie věd České republiky

Abstrakt: Objekt Sagittarius A* v centru Mléčné dráhy je nejbližší supermasivní černá díra v našem kosmickém okolí. Zde se odehrávají různé astrofyzikální procesy, díky nimž se v blízkosti jádra Galaxie objevují rozmanité struktury. Příkladem jsou rázové vlny, jež blíže studujeme v této práci. V úvodu nejprve stručně shrnujeme historii výzkumu galaktického jádra včetně objevu kompaktního objektu Sgr A* v radiových vlnových délkách. V hlavní části práce se zaměřujeme na zjednodušený model rázových vln vznikajících při nadzvukovém pohybu hvězdy vůči okolnímu prostředí a diskutujeme jejich změnu podél hvězdné orbity. Uvažujeme čtyři různé modely: (a) model bez přítomnosti pohybu plynného prostředí vytékajícího ze supermasivní černé díry nebo akreujícího na ni, (b) model s uvážením výtoku, (c) případ vtoku a nakonec (d) model kombinující zároveň vtok i výtok. Diskutujeme symetrie a asymetrie každého modelu a zjišťujeme, že model uvažující okolní prostředí v klidu se jeví symetrický vůči přechodu pericentrem. Naproti tomu kombinovaný model se vyznačuje největšími asymetriemi. Nakonec jsou pro všechny zmíněné modely uvedeny profily pro tečnou rychlost hmoty a plošnou hustotu hmoty v obálce rázové vlny pro různé body podél dráhy.

Klíčová slova: Jádro Galaxie; Astrofyzikální procesy; Rázové vlny; Mezihvězdní prostředí

Contents

Preface

But we must not forget that all things in the world are connected with one another and depend on one another, and that we ourselves and all our thoughts are also a part of Nature.

— Ernst Mach

Figure 1. The memorial plate of prof. Ernst Mach was placed at Carolinum building of Charles University in Prague at the occasion of the centenary of his death.

A memorial plate was placed on the wall of the historical building of Carolinum at the Charles University in Prague in honour of the eminent scientist, philosopher, and professor of experimental physics Ernst Mach.[1] Figure 1 shows the memorial plate that portraits prof. Ernst Mach together with an artistic representation of an emerging bow-shock wave – among important subjects of Ernst Mach where he contributed very significantly. In 1887, Mach took a photo that shows a bow-shock wave around a supersonic bullet and the memorial plate is based on this photo where the object in a triangular shape refers to the bow-shock wave and the head of Ernst Mach represents the supersonic bullet. Exactly these shock-wave structures occur frequently in Nature and they can be observed also near our Galactic centre which is the subject of this bachelor thesis.

Astronomy is not only considered to be the oldest Natural Science, but it is also included among the most modern and technically challenging disciplines. Nowadays it is more than common that with all the technical and science progress, professional as well as amateur astronomers are enriching general knowledge of the public with observations of different types of cosmic objects from those on the atomic level across dust particles, planets and stars to much larger objects, such as galaxies and clusters of galaxies. At the same time, astrophysics deals with physical processes, for instance motion, acceleration and structuring of matter, formation of planets, evolution of stars and innumerable mechanisms shaping the Universe.

[1] Ernst Mach, born 18^{th} of February 1838 in Chrlice (Brno), deceased 19^{th} of February 1916 in Vaterstetten, Munich. In 1867, Ernst Mach became Professor of Experimental Physics at the Charles University in Prague, where he taught and lectured another 28 years since then. During these years he was twice elected Rector of the University (in 1879/80 and 1883/84).

1. Introduction

1.1 Historical remarks about the Galactic centre research

We start our discussion with a brief overview of Galactic centre research in the historical context. The main content of the thesis will then focus on rather narrow selected topics. Unless stated otherwise, the following, mostly historical review is based on Sanders [2014].

Nowadays, it is generally accepted that the Universe consists of galaxies, and our Milky Way is one of them. The discovery of the Milky Way goes back to the 18^{th} century, precisely to the year 1750, when Thomas Wright proposed a model of the Milky Way as a spinning disk consisting of stars and the Earth was a part of this system [Wright, 1750] (a confirmation of this idea was made by William Herschel and his observations in 1785 [Herschel, 1785]). In 1755, Immanuel Kant suggested that the proposed structure of the system of stars in the centre of the Galaxy could have been made by the collapse of the gas cloud, afterwards the system of the stars was flattened and supported against its own gravity by rotation [Kant, 1755]. This idea was generally accepted by the year of 1930 due to the works of Jan Oort and Bertil Lindblad (Oort [1927a,b,c], Lindblad [1930]).

In 1876, professor Jacobus Cornelius Kapteyn measured the positions of more than 450 000 stars in the Southern Hemisphere. He devised his model of the Milky Way – the Kapteyn Universe – in which the Sun was placed exactly in the centre of the large stellar system consisting of stars Type II [Kapteyn, 1892]. In 1912, Henrietta Leavitt published her work on the relationship between absolute brightness and the period of periodic variable stars [Leavitt and Pickering, 1912] (their brightness varies regularly). She did this discovery by comparing the photographic plates of Large Magellanic Cloud (LMC). The distance of stars was then derived from the Leavitt's relationship, but only the relative one. Then, Harlow Shapley calibrated Leavitt's relationship and estimated that entire Milky Way was about 300 000 ly in diameter. He also calculated the distance r to the Galactic centre as $r \approx 9,7$ kpc [Shapley, 1939].

The Great Debate between Shapley and Curtis took place in 1920, when the mentioned participants tried to give the answer to the question not only about the absorption in the Universe but also about the existence of the Universe itself and what this term should stand for. Shapley claimed the Universe is the Milky way with its nearby satellites and Curtis thought that it is vastly larger with other possibly enormous galaxies like the Milky Way.

One of the astronomers who largely contributed to the discovery of the Galaxy was, previously mentioned, Jan Oort. Not only did he significantly lower the Shapley's estimated values for the distance to the Galactic centre and its rotation velocity at the position of the Sun, but he also determined that the centre is roughly in the direction of the constellation of Sagittarius and that the density in this direction is much higher than it is locally. This statement was made in 1960 in the work Oort and Rougoor [1960]. It was based on their 21 cm line observations and also on the radio wavelength observations made by R.X. McGee and J.G. Bolton, who discovered this Galactic radio source in 1954. According

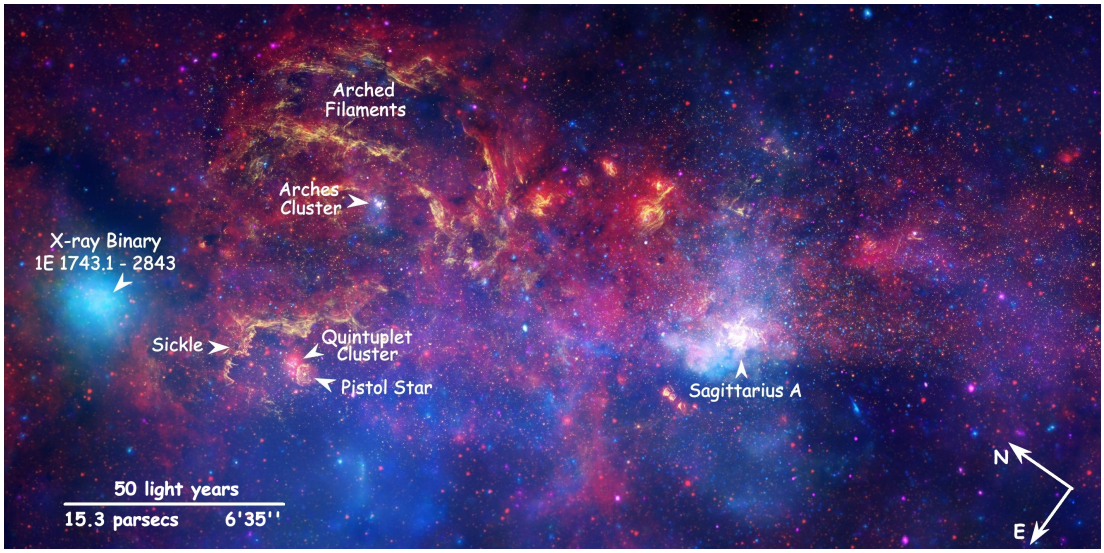

Figure 1.1. A composite multi-wavelength image of the centre of the Milky Way that covers in total about one-half a degree. The image was obtained with using infrared light from Spitzer satellite (encoded by red colour), X-rays from Chandra (blue), and optical wavelengths from the Hubble Space Telescope (yellow). The centre of the Galaxy (Sgr A*) is the bright region to the right of the middle (credit: NASA, ESA, SSC, CXC, and STScI).

to Oort's surveys of faint RR Lyrae variables near the Milky Way, the distance to its centre was calculated as $r \approx 8.7$ kpc [Oort and Plaut, 1975].

Between 1927 and 1938, Cecilia Payne-Gaposchkin became a technical assistant to Shapley, who was later also her supervisor of the Ph.D. thesis [Payne, 1925]. Among other things, she studied the spectral classification of stars, stellar atmospheres and temperatures, the abundances of elements etc. Gaposchkin discovered that the stars have very similar relative chemical abundances and that they comprise of hydrogen and helium from 99%.

Another big step in the evolution of the discovery of the Galaxy was its observing at radio wavelengths. In 1931, Karl Guthe Jansky was the very first person who observed in radio wavelengths. Ten years later, in 1941, Grote Reber completed the very first radiofrequency sky map. In the 1960s, it was generally accepted that the visible light is dimmed by the environment between the Solar system and the Milky Way, so the astronomers needed to start observing in infrared wavelengths. The very first near-infrared observations were carried out by Eric Becklin and Gerry Neugebauer [Becklin and Neugebauer, 1968]. It was expected that the stars closer to the Galactic centre come from the old population of giant stars. These giants have temperatures between 2500 and 4000 Kelvins and they are emitting largely the radiation from 1 to 2 microns, so called near-infared radiation. Although Becklin and Neugebauer detected a bright point infrared source near the Galactic centre, its colours were unrecognisable from the ones of the luminous giant stars.

The history of black holes (BH) goes back to the year 1916, when Karl Schwarzschild wrote a letter to Einstein with exact solutions of the Einstein field equations, where nowadays called black hole was a singular solution to these equations. In 1963, Maarten Schmidt analysed spectral lines of meantime unknown, but extremely luminous objects, later called "quasars", and found that their spectral lines are highly redshifted. It was clear that they were incredibly

distant objects, after all, they appeared to be star-like so astrophysicists tried to discover how these small and very distant objects can be so luminous. They probably need a powerful source of energy. In the 1970s, Donald Lynden-Bell and Martin Rees, independently from each other, made similar conclusions of the source fuelling the quasars. They proposed that there need to be an accretion onto a supermassive object, which resides in the centre and probably each galaxy does have one.

The stories about who actually used the term of the black hole for the first time point to the name Robert Dicke [Bartusiak, 2015], who was the physicist of the Institute for Advanced Study in Princeton. Dicke mentioned that the complete collapse of certain stars created the environment, where gravity was so strong that no light or matter could escape. He made a joke about comparing this unique object to the "Black Hole of Calcutta". This is set to be during the years 1959 and 1961. Few years later, in 1967, John Wheeler coined the term "black hole"in his talk at the AAS meeting in the New York City. Then, it became a frequently used word in the association with these massive objects.

In 1974, Bruce Balick and Robert Brown made a very important discovery and they are the very first ones that looked at the compact radio source in the centre of the Galaxy using a radio interferometer (NRAO) [Balick and Brown, 1974]. The radio source is nowadays known as Sagittarius A* (Sgr A*).

As far back as 1977, the estimation of the total mass of the cental parsec (pc) was set to $M_\bullet \sim 4 \times 10^6\ M_\odot$ [Wollman et al., 1977]. Between 1982 and 1998, Don Backer and Dick Sramek measured the proper motion of radio source Sgr A* and found that this object seem to reside at one place and this place is located in the centre of our Galaxy [Backer and Sramek, 1982]. Their discovery was then followed by the group of Mark Reid [Reid et al., 1999]. In 1982, George Rieke and Marcia Lebofsky suggested that in the inner few light years is a strong presence of a number of giant red stars. They also discovered that the Galaxy can be successfully compared to other spiral galaxies and not to other galaxies such as Seyfert galaxies etc. [Rieke and Lebofsky, 1982]. In the same year, Eric Becklin, Ian Gately, and Michael Werner revealed that inner 5 or 6 light years were relatively empty of interstellar dust and gas, however, between 6 and 15 light years appeared to be a ring of warm dust [Becklin et al., 1982]. Then, in 1983 Jan Oort had a talk on the Galactic nucleus at the meeting that took place in Groningen. Based on the previous suggestion of Rieke and Lebofsky, he pointed out that the ionization of the gas in the central few light years might not be caused by the presence of a massive black hole but it rather could be entirely explained by hot young stars formed in the core of the Galaxy about a million years ago [Oort, 1985]. Later, in 1983, Harvey Liszt, Butler Burton, and Thijs van der Hulst found that the ring located 6 to 15 light years away from the centre consists of a large fraction of neutral gas [Liszt et al., 1983]. They discovered that the ring rotates about the centre with velocity around 100 km/s.

In 1990, it was discovered that many of the massive stars near Sgr A* emitted an emission spectral line from neutral helium at 2 microns. This is typical for young blue supergiant stars that are loosing mass through winds. The fact that these very young blue supergiants form a compact cluster in the inner few light years was discovered in 2000s by the group led by Reinhard Genzel, followed soon by Michael Burton and David Allen. Simply said, in the inner few light years

older red supergiants are being observed, but if we go closer to the actual BH, the number of red supergiants decreases and the number of younger blue stars increases (for more about this "Youth Paradox", see Ghez et al. [2003]). But more interesting question was how these massive young stars can be formed so close to the BH? As the concept of the star formation itself can be imagined a model of a cloud falling into a gravitational field resembling the Galactic centre with a central point mass of 2.5 million solar masses [Sanders, 1998]. Firstly, the cloud wrap around the BH, it self-collides and forms an elliptical ring that maintains its shape as it precesses around the centre for up to million years. Presumably, it is the self-collision that forms strong shocks and mainly the stars. Because of the collapse of cloud into a disk, the stars are then found in a disk in the Galactic plane. These stars are also found on highly elliptical orbits, as it was later discovered by observations.

At the turn of the millennium, astronomers from Europe (led by Reinhard Genzel) and astronomers from the US (led by Andrea Ghez) started to measure the proper motions of stars near the centre of the Galaxy. They were able to measure the actual orbits of individual stars and also the radial velocity of the stars (the component of velocity along the line of sight) due to the strong helium emission line from the young complex of stars near Sgr A*. In 1995, Genzel with his group found that the radial velocity was increasing toward the centre and this was an evidence for a mass concentration within one and one-half light months. In 1996, Eckart and Genzel published a paper with proper motions of 39 stars [Eckart and Genzel, 1996]. It was for a time baseline of 4 years and the stars were located within a projected distance of 1/10 of one light year from the Galactic centre. In 1998, the number of stars, for which were measured proper motions, was doubled by the group of Ghez [Ghez et al., 1998]. The stars were located within $4''$ of Sgr A* and since that time they started to be recognised as "S"stars. In 2000, it was proven by UCLA group of Ghez that the acceleration vectors pointed directly back to Sgr A* as the location of the centre of force [Ghez et al., 2000]. In the same year, Genzel et al. continued in their measurements of proper motions and they discovered that the stars seemed not to be moving in all directions but exhibited a clockwise pattern of circular motion about the centre [Genzel et al., 2000]. Three years later, Yuri Levin and Andre Beloborodov found that the stars appeared to lie in a single plane disk which was significantly rotating [Levin and Beloborodov, 2003]. As these stars were proven to be very young, Levin and Beloborodov assumed they were formed one or two million years ago in a dense gaseous accretion disk. The disk was assumed to be formed by the central black hole or ejected in the star formation/accretion event, leaving only the remnant of stars.

Both Genzel's and Ghez's groups made a great progress in the estimation of the accurate orbits of the stars that were located closest to the Galactic centre. This progress was very important for the proof that stars orbit a heavy, dark compact object. Their best estimates for the central mass were between 3.6–3.5 million solar masses. This estimation was later set to 4–4.5 million solar masses [Ghez et al., 2008].

Understanding processes in the Galactic centre is crucial for the understanding of processes in distant galaxies, other than Milky Way, which are also hosts of black holes (see for example Markoff et al. [2015], Markoff [2013a,b] or Lang et al.

[2014], Lang and Drout [2011], Lang et al. [2010]).

In all past observations and discoveries, astronomers tried to find what was the supermassive radio source, around which the other objects/stars seemed to orbit. They considered many options as for example purely fermion/boson stars or neutron stars, which should reside in the centre of the Galaxy. But various previously mentioned observations edged out these options and they all seemed to point out to the one specific object – black hole, an object at that time believed to be hypothetical and so far considered only as a mathematical singularity of Einstein's field equations.

1.2 Structures near the Galactic centre

As we know today, a supermassive black hole (SMBH) is located in the centre of the Milky Way at the position associated with the compact radio source Sagittarius A* (Sgr A*). Its location is at the distance of ~ 8 kpc from the Earth with the mass of $M_\bullet \sim 4 \times 10^6\ M_\odot$, where $M_\odot$ stands for the mass of the Sun. At that distance, one arc second corresponds to ~ 0.04 parsec. In general, SMBHs

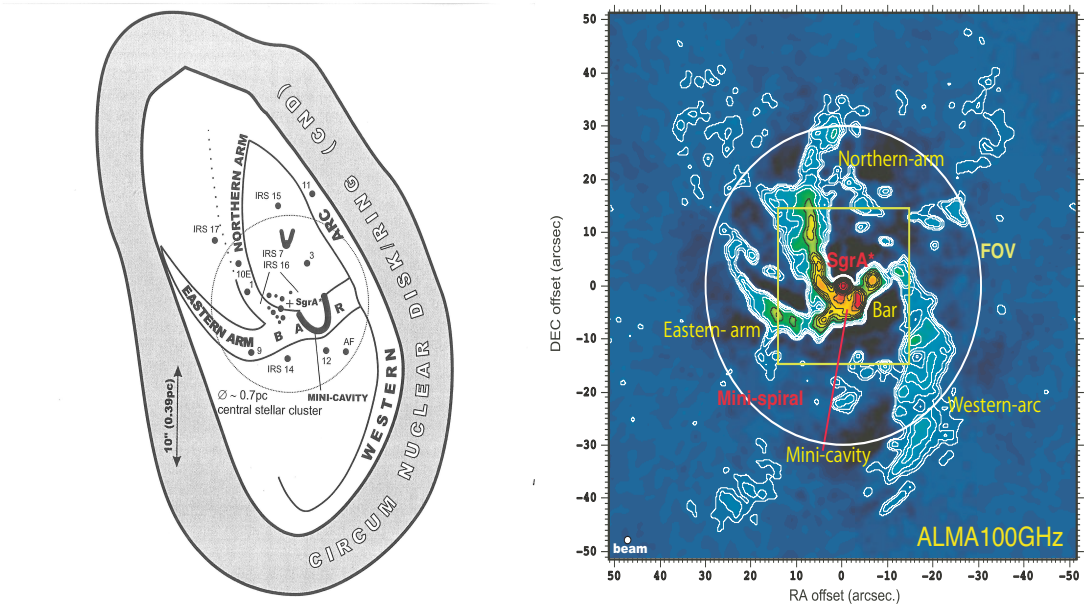

Figure 1.2. *Left*: An illustration of the central parsec of the Milky Way enclosed by CND [Eckart et al., 2005]. *Right*: A radio interferometric ALMA map of gaseous streamers in the Mini-spiral region in millimetre wavelengths [Tsuboi et al., 2016].

probably reside in nuclei of most galaxies and they are often identified by the accretion of the material onto them or by jets and the wind launching in their neighbourhood. Astrophysical black holes are usually not isolated objects but they are rather surrounded by dusty and gaseous environment along with stars, even star clusters and coherent structures, such as filaments, shocks, and gaseous and dusty streamers, namely, the Mini-spiral and Circum-Nuclear Disk (CND) near Sgr A*. Left panel of Fig. 1.2 represents the central parsec of the Galaxy enclosed by an association of clouds/filaments of dense (10^4 – 10^7 cm^{-3}) and warm (several hundred Kelvin) molecular gas. Moreover, it captures the very closest environment of Sgr A* (Northern and Eastern arms, Western arc, mini-cavity, the

nuclear star cluster and more). Among those gaseous structures are bow shocks that are the main study of this thesis.

1.3 Bow-shock waves

Bow-shock waves are common structures in Nature. When a duck paddles across the pond, and when it is fast enough (i.e. faster than the corresponding speed of wave propagation – gravity waves in this case), water in front of it merges into a V-shaped wall surrounding the speeding animal (left panel of Fig. 1.3). It

Figure 1.3. *Left*: The German duck in the pond with an illustration of a surface wave pattern that it generates (credit: M. Zajaček). *Right*: A supersonic expansion fan around a jet (credit: D. Andrejczuk).

is similar with boats or any other object as well. Supersonic velocities are also common in the atmosphere (sound waves in this case), e.g. when a supersonic flow turns around a convex corner (see right panel of Fig. 1.3. This so-called expansion fan consists of an infinite number of Mach waves.

The shock waves are generated by the surface of the object. It is the process

Figure 1.4. *Left*: A bow-shock structure (red arc-shaped cloud of dust and gas) that surrounds the bright supergiant star Alpha Camelopardalis (α Cam) situated in the middle of the image. The image is from NASA's Wide-field Infrared Survey Explorer (WISE) (credit: NASA/JPL-Caltech/UCLA). *Right*: An infrared L′-band image of the bow-shock structure around IRS 8 star in the Galactic centre from ESO VLT UT4 telescope [Rauch et al., 2013].

that creates drag force and slows down the object. The mechanism is analogical to bow shocks in the Universe. Stellar bow shocks (see Fig. 1.4) are formed due to the supersonic motion of a star in the interstellar medium (ISM). The stellar wind interacts with the ISM and the whole process is thus more complicated and it creates cometary structures that can be observed. Although the observations are difficult because of the large distance of cosmic objects and the finite bow-shock thickness in the astrophysically realistic situations, it does not prevent the astronomers from the research about this important phenomenon which can provide us with evidence about as yet undetected population of fast-moving compact stars. For more see Sec. 2.1. Probably the largest of such bow-shock structures is The Bullet Cluster (1E 0657-558) which is about one Mpc across. It consists of two colliding clusters of galaxies.

1.4 Outline of the thesis

The main focus of this bachelor thesis concerns the Milky Way, in particular its centre, which is the host to the SMBH Sgr A*. Another aim of this thesis is in the understanding and analysing shock waves that occur near stars of different properties due to their supersonic translational velocity with respect to the ambient medium in a combination with stellar winds. The thesis is organised as follows.

In Chapter 1 we introduce the subject and also give a historical review of its discovery. Given a limited volume of this thesis, we focus on a particularly important and timely example of previously mentioned structures, namely bow shocks that develop ahead of fast-moving stars embedded within a diluted ambient medium.

In Chapter 2 we give some basic relations for the shape of the bow-shock shell, the tangential velocity in the shell and the mass surface density of the shell. We also discuss the ambient medium in the vicinity of the Galactic centre.

Our main results are described in Chapter 3. We worked out models both for constant and radial-dependent densities of the ambient medium, and we also considered models with only central outflow from the SMBH, central inflow onto SMBH, or the combined model consisting of both. In the inner areas, the gravitational force of the black hole is so strong that the mass flows inward and feeds the black hole. From an energetic point of view, the most probable scenario for outflow is that the gaseous and dusty clouds are blown away at the longer distance by the energetic winds from supernova remnants when the star formation occurs. This is a possible mechanism which could cause outbursts from the outer areas of SMBH. All models were considered in the approximation of radial symmetry.

In Chapter 4 we give a compact discussion of our results and whether they are observable with nowadays telescopes with defined angular resolution.

Main results of this work and our future prospects are summarized in Chapter 5. Appendices provide a more detailed description of several technical aspects.

2. Bow-shock Structures

2.1 Thin axisymmetric bow shocks

We briefly mentioned bow shock waves in Introduction. These gaseous cometary structures occur when the wind-blowing stars move supersonically with respect to the ambient medium (we assume the medium is uniform). In our model (based on Wilkin [1996]) is put an emphasis on the conserved internal momentum within the shell of the bow shock. Due to the supersonic velocity, the pressure forces can be neglected.

The radial outflow of ionized gas ejected from the star, referred to as the stellar wind, collides with the interstellar medium (ISM). After that the wind is decelerated. It leads to two layers of shocked gas but these are expected to mix and due to the effective post-shock cooling the thickness of the layers is negligible in the comparison with the distance to the star. Based on this, we simplify our model in the thin-shell limit.

In the hydrodynamic approximation, the medium can be described as the continuous fluid with its velocity $\boldsymbol{v}$, temperature T and density ρ. Then the general hydrodynamical equations, valid for the fluid, are: the continuity equation (mass conservation), (2.1), the first law of thermodynamics and the equation of state,(2.2) , the Euler equation (conservation of momentum),(2.3) ,and the energy equation, (2.4) (lecture notes, V. Karas, 1996: *Astrophysical Analogies: From Quasars to Pulsars*, Sec. 3.2) .

$$\frac{\partial \rho}{\partial t} + \nabla \cdot (\rho \boldsymbol{v}) = 0 \ , \tag{2.1}$$

$$dQ = TdS - Pd\left(\frac{1}{n}\right) \qquad P \equiv P(\rho, S) \ , \tag{2.2}$$

where P stands for pressure, S is entropy density and $n = \rho/m$ is the particle number density,

$$\rho \frac{\partial \boldsymbol{v}}{\partial t} + \rho \boldsymbol{v} \cdot \nabla \boldsymbol{v} = -\nabla P + \boldsymbol{f} \ , \tag{2.3}$$

where $\boldsymbol{f}$ refers to external force density,

$$\frac{\partial}{\partial t}\left(\frac{1}{2}\rho v^2 + \rho w\right) + \nabla \cdot \left[\left(\frac{1}{2}\rho v^2 + \rho w + P\right)\boldsymbol{v}\right] = \boldsymbol{f} \cdot \boldsymbol{v} - \nabla \cdot \boldsymbol{F_{rad}} - \nabla \cdot \boldsymbol{q} \ , \tag{2.4}$$

where $\boldsymbol{F_{rad}}$ is the vector of radiation flux, $\boldsymbol{q}$ is the conductive flux of heat which measures the transport of thermal energy and ρw has a meaning of thermal energy per unit volume.

If we specify to the bow-shock scheme (from a microscopic point of view), when the stellar wind is described by hydrodynamic equations (see also Baranov et al. [1971] and Wilkin [1996]), the collision of the stellar wind and ISM is as follows. The ions of the stellar wind may be considered as probe particles moving in the field of charged particles of the ISM. Through this interaction the ions almost completely lose their directed momentum and transfer it to the particles of the interstellar plasma, which in turn, exert a drag on the ions of the stellar

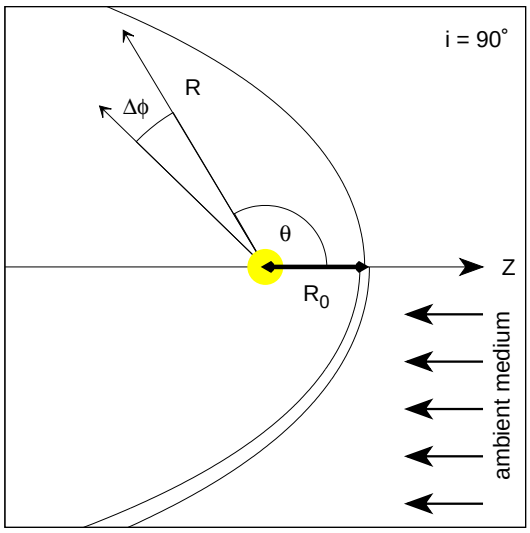

Figure 2.1. An illustration of the bow-shock shell given by eq. (2.8). In the star co-moving frame, the star (yellow dot) resides at the coordinate origin and the stellar wind blows in the radial direction from the star, z-axis is the symmetry axis of the shell. The ambient medium moves in the opposite direction of the axis z. Parameter R_0 stands for the standoff distance given by eq. (2.7), $\Delta\phi$ is azimuthal angle about the symmetry axis, i is the inclination angle, R and θ are polar coordinates. The upper half of the figure illustrates the bow shock in the thin-shell limit while the shell in the lower half has some non-vanishing thickness. In this work we assumed the former case of the thin-shell limit due to the effective post-shock cooling.

wind [Baranov et al., 1971]. In Fig. 2.1 the z-axis is the axis of symmetry of the bow shock shell, θ is the polar angle from the axis of symmetry seen by the star at the coordinate origin, R is a radius vector from the centre of the star and $\Delta\phi$ is azimuthal angle about the symmetry axis. In the reference frame of the star, let $-\boldsymbol{z}$ be the direction of the ambient medium. When bow-shock structures are being observed, they can head to different directions and it depends on the inclination angle. When the inclination angle $i = 0$, observer is looking directly at the apex of bow-shock shell. If $i = 90°$ the line of sight is perpendicular to the axis of symmetry of bow shock. In this work the inclination angle is set to 90°. When the isotropic stellar wind and ISM collide head-on at $\theta = 0$, the collision needs to be described by the balance of the ram pressures

$$\rho_{\mathrm{w}} V_{\mathrm{w}}^2 = \rho_{\mathrm{A}} V^{\star 2} \,, \tag{2.5}$$

where ρ_{w} is the desity of the stellar wind, V_{w} is the terminal velocity of the stellar wind, the star moves with constant velocity of magnitude $V^\star$ with respect to the uniform medium of density ρ_{A}.

We can write the mass rate $\dot{m}_{\mathrm{w}}$ of the isotropic stellar wind in the distance R_0 from the star as

$$\dot{m}_{\mathrm{w}}(R_0) = \rho_{\mathrm{w}}(R_0) V_{\mathrm{w}} 4\pi R_0^2 \,, \tag{2.6}$$

where $4\pi R_0^2$ refers to the area of the flow of the mass, when the wind ejection from the star is considered to be isotropic. Head-on collision is described by the conditions $\theta = 0$ and $R(0) = R_0$. The radius R_0 is often referred to as the standoff distance of the bow shock and it can be derived from the eq. (2.5) using eq. (2.6)

as

$$R_0 = \sqrt{\frac{\dot{m}_{\rm w} V_{\rm w}}{4\pi \rho_{\rm A} V^{\star 2}}} \,. \tag{2.7}$$

The standoff distance R_0 is the parameter which scales the size of the bow shock (it sets the length scale of the shell) and it generally depends on four parameters: $\dot{m}_{\rm w}$, $V_{\rm w}$, $V^{\star}$ and $\rho_{\rm A}$. After the mathematical formulation of the problem (for more details see Wilkin [1996]) we obtain formulae for the function of the shape of the shell, eq. (2.8), mass surface density, eq. (2.9), and tangential velocity of shocked gas at all points in the shell, eq. (2.10), as a function of θ:

$$R\left(\theta\right) = R_0 \csc\theta \sqrt{3\left(1 - \theta\cot\theta\right)} \,, \tag{2.8}$$

$$\sigma\left(\theta\right) = R_0 \rho_{\rm A} \frac{\left[2\alpha\left(1-\cos\theta\right) + \varpi^2\right]^2}{2\varpi\sqrt{\left(\theta - \sin\theta\cos\theta\right)^2 + \left(\varpi^2 - \sin^2\theta\right)^2}} \,, \tag{2.9}$$

$$v_{\rm t}\left(\theta\right) = V^{\star} \frac{\sqrt{\left(\theta - \sin\theta\cos\theta\right)^2 + \left(\varpi^2 - \sin^2\theta\right)^2}}{2\alpha\left(1-\cos\theta\right) + \varpi^2} \,, \tag{2.10}$$

where $\alpha \equiv V^{\star}/V_{\rm w}$ is a non-dimensional parameter and $\varpi^2 = 3\left(1 - \theta\cot\theta\right)$ is a normalized cylindrical radius obtained from eq. (2.8). If we consider that the wind ejection from the star is not isotropic but confined in a cone of solid angle $\Omega = 2\pi(1-\cos(\theta_0))$, according to Zhang and Zheng [1997], the standoff distance is then given by

$$R_0 = \sqrt{\frac{\dot{m}_{\rm w} V_{\rm w}}{\Omega \rho_{\rm A} V^{\star 2}}} \,, \tag{2.11}$$

where the matter is ejected in the opening angle of $2\theta_0$.

We need to mention that for $\theta = 0$ the eq. (2.8) has an asymptotic behaviour, but this is not the actual singularity. The Taylor series for R(θ) about $\theta = 0$ yields $\approx R_0(1 + \theta^2/5 + 29\theta^4/1050)$ where the order of correction is given by Baranov et al. [1971].

We can take a closer look to eq. (2.7) and derive the relation between the size of the standoff distance at the apocentre ($R_{0\rm Apo}$) and at the pericentre ($R_{0\rm Per}$) directly from this equation (M. Zajaček, 2016, private communication). The ratio of the sizes is then given by

$$\frac{R_{0\rm Apo}}{R_{0\rm Per}} = \left(\frac{\rho_{\rm APer}}{\rho_{\rm AApo}}\right)^{1/2} \frac{V^{\star}{}_{\rm Per}}{V^{\star}{}_{\rm Apo}} \,. \tag{2.12}$$

This ratio is valid for the case when the mass flow rate $\dot{m}_{\rm w}$ and the velocity of stellar wind $V_{\rm w}$ are assumed to be constant during one orbital period. Slightly different relation for this ratio can be obtained if another two assumptions are considered. At first we use relation $\rho_{\rm A} = \mu m_{\rm H} n_{\rm A}$, where $n_{\rm A}$ stands for the number density of an ambient medium near the Galactic centre, $m_{\rm H}$ is the mass of hydrogen atom and μ is the relative molecular mass. We assume that $n_{\rm A}$ is a function of the distance r from the BH and it has a power-law form expressed as

$$n_{\rm A} = n_{\rm A0} \left(\frac{r_0}{r}\right)^{\gamma} \,, \tag{2.13}$$

where n_{A0} and r_0 are parameters of the profile and γ is the power-law index that lies in the interval (0,2). The second assumption is that the relative velocity of the star $V^\star$ is approximately the same as the orbital velocity of the star around the Galactic centre, $V^\star = V_{\mathrm{orb}}$.

After these assumptions we obtain the ratio of the standoff distances as the ratio of the distances and the velocities of the star at the apocentre and at the pericentre as

$$\frac{R_{0\mathrm{Apo}}}{R_{0\mathrm{Per}}} = \left(\frac{r_{\mathrm{Apo}}}{r_{\mathrm{Per}}}\right)^{\gamma/2} \frac{V_{\mathrm{orbPer}}}{V_{\mathrm{orbApo}}} \,. \tag{2.14}$$

If we use the formulae from classical celestial mechanics for the ratio of distances $(r_{\mathrm{Per}}/r_{\mathrm{Apo}})$ = (1-e)/(1+e) and the ratio of velocities $(V_{\mathrm{orbPer}}/V_{\mathrm{orbApo}})$ = (1+e)/(1-e), where e is an eccentricity of a general elliptical orbit, we obtain the ratio of $R_{0\mathrm{Apo}}$ and $R_{0\mathrm{Per}}$ only as a function of two parameters – the orbital eccentricity e and the power-law index for the ambient density distribution γ. The relation is then given by

$$\frac{R_{0\mathrm{Apo}}}{R_{0\mathrm{Per}}} = \left(\frac{1+e}{1-e}\right)^{1+\gamma/2} \,. \tag{2.15}$$

In Tab. 2.1 are summarized values of the ratio $\frac{R_{0\mathrm{Apo}}}{R_{0\mathrm{Per}}}$ for different values of the eccentricity and the power-law indices. We can notice that the circular orbit, for which $e = 0$, is characterized by the same standoff distance at the pericentre and simultaneously at the apocentre for each value of the parameter γ.

e	γ	$R_{0\mathrm{Apo}}/R_{0\mathrm{Per}}$
0	any	1
0.5	1	5.2
0.9	2	361
0.9	1	82.8
0.9	0.5	39.7
0.9	0	19

Table 2.1. Different values of the ratio $\frac{R_{0\mathrm{Apo}}}{R_{0\mathrm{Per}}}$ for selected exemplary values of parameters e and γ. The values of this ratio were computed using eq. (2.15).

2.2 Ambient medium

The density of an ambient medium plays also an important role in the scaling of the size of bow shocks. If we derive the density of an ambient medium assuming the hydrostatic equilibrium near the Galactic centre, the density decreases exponentially. For the demonstration of the behaviour of an ambient medium we use the Eulerian description of the motion of the continuum considering the array of velocity vectors [Langer and Podolský, 2013]. Then the Euler equation is

$$\frac{\partial \boldsymbol{v}}{\partial t} + (\boldsymbol{v} \cdot \nabla)\boldsymbol{v} = \boldsymbol{a} \,, \tag{2.16}$$

where $\boldsymbol{v}$ refers to the velocity of the continuum and $\boldsymbol{a}$ is its acceleration. From the Newton's second law $\boldsymbol{a} = \boldsymbol{f}$, where $\boldsymbol{f} = \boldsymbol{f}(r)$ is the force density (specifically the

density of radially symmetric gravitational force exerted by SMBH of the mass $M_\bullet$ onto the star). The force density is given by

$$\boldsymbol{f} = \frac{1}{\rho_\mathrm{A}} \nabla P + \frac{GM_\bullet}{|\boldsymbol{r}|^2} \frac{\boldsymbol{r}}{|\boldsymbol{r}|} \,, \tag{2.17}$$

where ρ_A is the density of an ambient medium, $\boldsymbol{r}$ as a distance from the SMBH, P stands for pressure, G is the gravitational constant, $M_\bullet$ is the mass of the SMBH.

In the case of the hydrostatic equilibrium the acceleration is assumed to be trivial ($\boldsymbol{a} = 0 = \boldsymbol{f}$) so from eq. (2.17) we obtain

$$\nabla P = -\frac{GM_\bullet \rho_\mathrm{A}}{|\boldsymbol{r}|^2} \,. \tag{2.18}$$

We suppose the continuum is formed by an ideal gas and that the whole process of motion is isothermal (usually $T_\mathrm{A} \approx 10^4$ for HII region). Using the equation of state for the ideal gas and equation for the density of the ambient medium we obtain

$$\frac{dn_\mathrm{A}}{dr} k_\mathrm{B} T_\mathrm{A} = -GM_\bullet m_\mathrm{H} \mu \frac{n_\mathrm{A}}{|\boldsymbol{r}|^2} \,, \tag{2.19}$$

where n_A is the number density of the ambient medium, k_B is the Boltzmann constant, T_A is the temperature of the ambient medium, m_H is the mass of hydrogen atom and μ is the relative molecular mass. In eq. (2.19) we used a formula for the density of the ambient medium $\rho_\mathrm{A} = \mu m_\mathrm{H} n_\mathrm{A}$. After the separation of variables and integration from the Schwarzschild radius r_s (still in Newtonian framework) to an actual position vector of magnitude r, we finally get the number density profile of the ambient medium in the hydrostatical equilibrium as

$$n_\mathrm{a0} = \frac{n_\mathrm{A}(r)}{n_\mathrm{A}(r_\mathrm{s})} = \exp\left[-\frac{GM_\bullet m_\mathrm{H} \mu}{k_\mathrm{B} T_\mathrm{A}} \left(\frac{1}{r_\mathrm{s}} - \frac{1}{r} \right) \right] \,. \tag{2.20}$$

In eq. (2.20) $r_\mathrm{s} = \frac{2GM_\bullet}{c^2}$, where c is the speed of light. Based on observations [Wang et al., 2013], the density nearby Sgr A* seems to decrease with an increasing radius as $\sim 1/r$. In conclusion, we can then assume that the hydrostatic equilibrium does not occur near the Galactic centre and it should be taken as an approximation.

As it was mentioned in the outline of this thesis (see Sec. 1.4), we worked out models for bow shocks nearby Sgr A* assuming the ambient medium at rest, outflow from the SMBH and inflow onto the the SMBH, as well as the combined model of both. The parameter in the right panel of Fig. 2.2, r_B, is so-called Bondi radius [Bondi, 1952], which defines the region of gravitational accretion onto a spherically symmetric central body. It can be calculated as

$$r_\mathrm{B} = \frac{GM}{c_\mathrm{s}^2} \,, \tag{2.21}$$

where G is the gravitational constant, M is the mass of the body (in our case it represents the mass of Sgr A*, also referred to as $M_\bullet$), and c_s is the velocity of sound in the gas at infinity.

At infinity, gas is assumed to be at rest and of uniform density ρ_∞ and pressure p_∞. Then the square of sound speed is calculated as $c_\mathrm{s}^2 = \gamma p_\infty / \rho_\infty$, where γ is

a constant $1 \leq \gamma \leq 5/3$ [Bondi, 1952]. The models are illustrated in Fig. 2.2. Inside a spherical volume of the Bondi radius r_{B} we assume radial inflow of the mass towards the SMBH, outside this radius we assume radial outflow of the mass from the SMBH. Exactly at the radius r_{B} the ambient medium is at rest. Inside the radius r_{B} gravity of the SMBH is dominant, and the ambient medium accretes onto the supermassive BH. Outside of it we assume that the mechanical energy is deposited through stellar winds and supernovae. It is then thermalized via random collisions of the gaseous streams from neighbouring sources, and this results in a high temperature and a high thermal pressure that lead to a fast outflow of the injected matter [Silich et al., 2008].

X-ray emission of Sgr A* was studied in Wang et al. [2013]. The studies were based on 3 megaseconds of Chandra observations and it was observed that the Bondi radius for the Milky Way is approximately 4 arcsecond ($\approx$ 33 000 au).

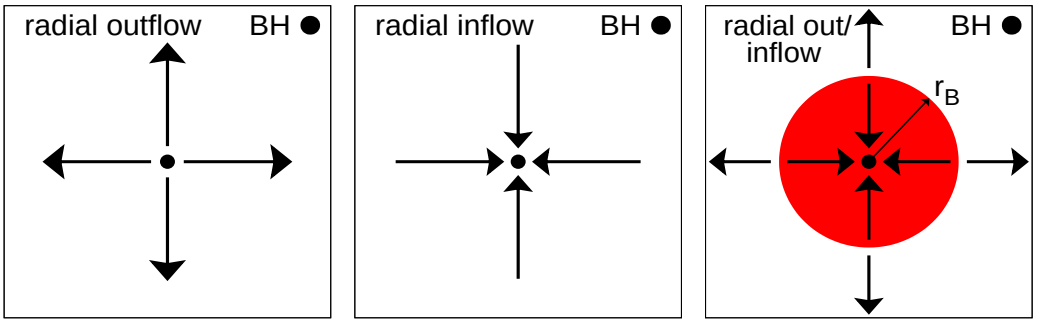

Figure 2.2. *Left*: The radial outflow of the mass onto the SMBH. *Centre*: The radial inflow of the mass onto the SMBH. *Right*: Combined model of the outflow from and the inflow onto the SMBH that are matched at the Bondi radius $r = r_{\mathrm{B}}$.

3. Results

Following results were inspired by Zajaček et al. [2016], where an effect of isotropic outflow from the Galactic centre on the axisymmetric bow shocks, with given shape by Wilkin [1996], was discussed. Here we present extra models of the inflow onto the supermassive black hole (SMBH) and the combined model taking simultaneously both, the outflow from and the inflow onto the SMBH, into account.

In Tab. 3.1 we give constants which were frequently used in the numerical calculations in the thesis.

quantity	**variable**	**value**	**dimension (SI)**
speed of light	c	2.99792458	10^{8} m s^{-1}
astronomical unit	au	1.495978707	10^{11} m
light year	ly	9.460730473	10^{15} m
parsec	pc	3.085677581	10^{16} m
constant of gravitation	G	6.67428	10^{-11} m^{3} kg^{-1} s^{-2}
mass of Sun	$M_{\odot}$	1.988497012	10^{30} kg
mass of Sgr A*	$M_{\bullet}$	7.953988048	10^{36} kg
Boltzmann constant	k_B	1.380 6503	10^{-23} m^{2} kg s^{-2}K^{-1}
mass of hydrogen atom	m_H	1.6735	10^{-21} kg

Table 3.1. Table of the main constants relevant in this work. Constants c, au, G are taken from Luzum et al. [2011]. For the calculation of the light year was used Julian astronomical year (1 year = 365.25 days). The mass of the Sun was obtained from the Third Kepler's law. For the mass of the SMBH we used a relation $M_{\bullet} = 4 \times 10^{6} M_{\odot}$. The mass of hydrogen atom was calculated using constants from Mohr and Taylor [1999] and from this paper we also used the value for Boltzmann constant.

3.1 Elliptic orbit and supersonic velocity

In Fig. 3.1 the orbits of stars from S-cluster, which are located (1–2)″ from the Galactic centre, are plotted. The true shape of the orbits in the potential of a point mass is known from the time of Kepler: the orbits have an elliptical shape with the centre of attraction at one focus of the ellipse. The orientation and the inclination angle of true orbits in three dimensions can be determined from the difference in the position of an apparent focus from that of Sgr A*, when the ellipses in three dimensions are projected into ellipses on the plane of the sky. If the mass distribution deviates significantly from the point mass, then elliptical orbits precess. In our case we simplified the model to the Newtonian approximation and we used only one orbit in the analysis, so we do not need to consider any precession. We neglected relativistic effects because, as it is clearly seen in Fig. 3.3, we considered an orbit of an object which is located $\approx 10^{3} r_{\mathrm{s}}$ away from the SMBH. Orbital elements for the orbits from Fig. 3.1 were obtained from Gillessen et al. [2009], Gillessen et al. [2013] and Meyer et al. [2012]. One of these orbits belongs to DSO/G2 (Dusty S-cluster Object) (for more, see Zajaček et al.

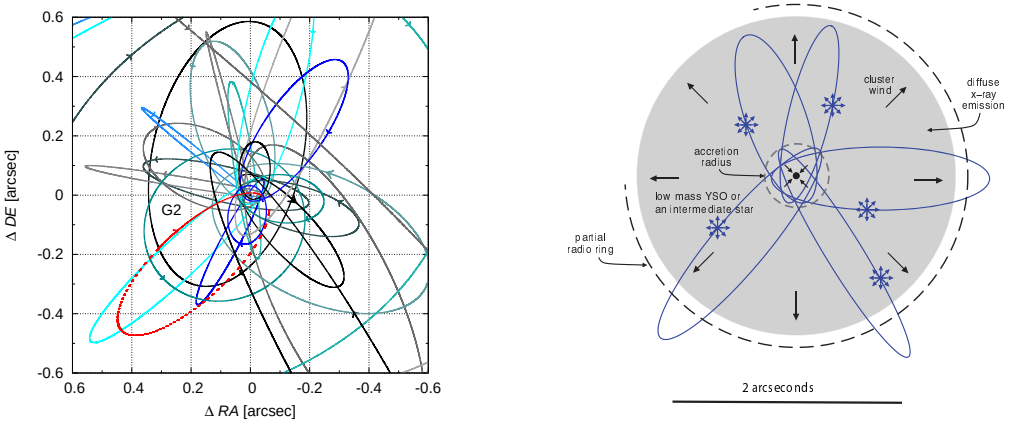

Figure 3.1. *Left*: A schematic diagram of the S-cluster stars in the centre of the Galaxy (Sgr A*). Orbital elements have been adopted from Gillessen et al. [2009], Gillessen et al. [2013], Meyer et al. [2012], and illustrated by Zajaček [2014]. *Right*: A schematic diagram of the emission of the central S-cluster stars embedded in the ambient medium of gas accreted onto from a spherical region of the sphere of SMBH influence. The diffuse wind originates from massive stars that are loosing their mass and from accretion disks of young low-mass stars that orbit the central SMBH Sgr A*. Figure is adopted from Yusef-Zadeh et al. [2016].

[2016], Zajaček et al. [2015], Valencia-S. et al. [2015], Eckart et al. [2014]). In Fig. 3.2 we plotted orbits for some of the sources, e.g. DSO/G2, S1 and S2 stars.

The orbits were computed using a program described in the Appendix A. We used orbital elements of DSO/G2 object for further analysis, but we will refer to it as the fiducial S-star. The main reason behind this lies in the analysis of the outflow and the combined models. If we used real parameters and observations for DSO/G2, the whole model would only be considered as the inflow model because the real Bondi radius for our Galaxy was observed as $\approx 33\,000$ au [Wang et al., 2013]. So our computations for the outflow and the combined model are not relevant for the real DSO/G2. Furthermore, our models are simplified to the star – Sgr A* system but DSO/G2 is more complicated object with a a little bit disputable nature (for more about DSO/G2 structure, see Sec. Introduction in Zajaček et al. [2015]).

Some of the main characteristic parameters of objects in graphs 3.2 and 3.3 are in Tab. 3.2. For computing the orbit of DSO/G2 (later in the analysis of different flow models referred to as the fiducial S-star) we used orbital elements from Valencia-S. et al. [2015]. Eccentricity e, period of one orbit T, as well as the value of the semi-major axis a of objects S1 and S2 are obtained from Eisenhauer et al. [2005] and Gillessen et al. [2009], respectively. The index *per* refers to the pericentre and the index *apo* to the apocentre. The distances at the pericentre and at the apocentre were computed as

$$r_{\mathrm{per}} = a(1-e)\ , \tag{3.1}$$

$$r_{\mathrm{apo}} = a(1+e)\ . \tag{3.2}$$

For the velocities we used following formulae

$$v_{\mathrm{circ}} = \sqrt{\frac{GM_\bullet}{r}}\ , \tag{3.3}$$

$$v_{\mathrm{parab}} = \sqrt{2}\cdot v_{\mathrm{circ}}\ , \tag{3.4}$$

$$v_{\mathrm{elip}} = \sqrt{GM_{\bullet}\left(\frac{2}{r} - \frac{1}{a}\right)}\,. \tag{3.5}$$

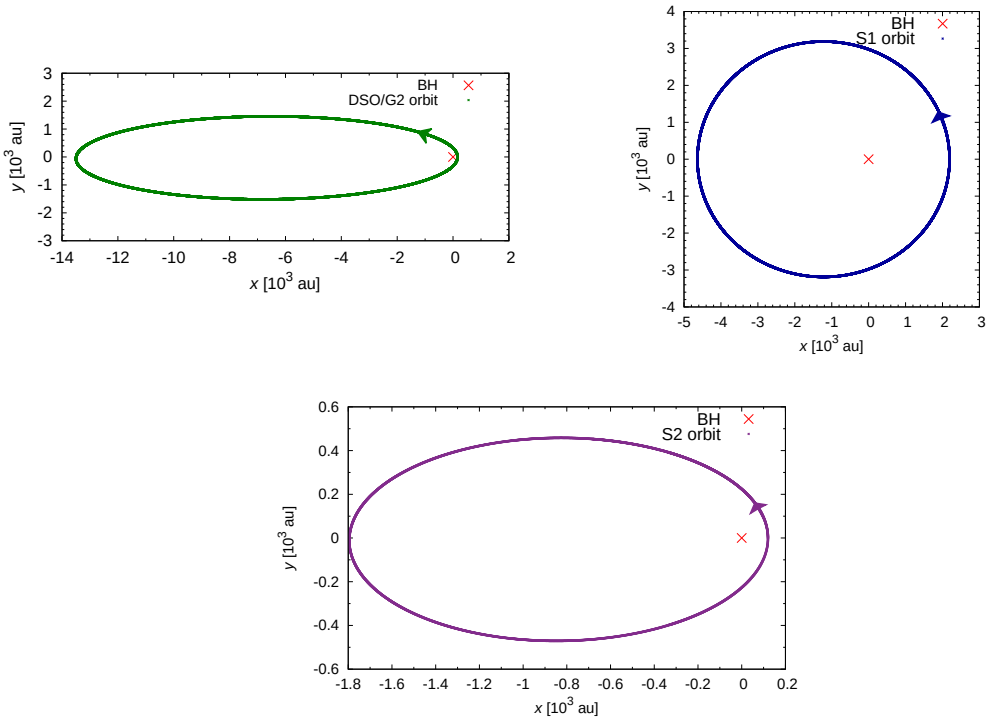

Figure 3.2. An illustration of the de-projected elliptic orbits of DSO/G2 object (top left panel), S1 (top right panel) and S2 (bottom centre panel) stars. The main parameters are given in Tab. 3.2.

	DSO/G2	**S1**	**S2**
a [″]	0.825 ± 0.075	0.412 ± 0.024	0,1246 ± 0.0019
e	0.976 ± 0.001	0.358 ± 0.036	0.8831 ± 0.0034
T [year]	262 ± 38	87.8 ± 18.8	15.56 ± 0.35
r_{per} [au]	163 ± 16	2182 ± 176	120 ± 4
r_{apo} [au]	13450 ± 1223	4616 ± 295	1936 ± 30
v_{per} [km/s]	7019 ± 355	1486 ± 91	7457 ± 130
v_{apo} [km/s]	85 ± 7	703 ± 82	463 ± 83

Table 3.2. Main characteristics of the orbits of the different sources: semi-major axis a, excentricity e, period of one orbit T, distance of the star from the SMBH at the pericentre r_{per} or at the apocentre r_{apo}, orbital velocities at the pericentre v_{per} and at the apocentre v_{apo}. Parameters for S1 and S2 objects were used in Fig. 3.3. Orbital elements for S1 and S2 were obtained from Eisenhauer et al. [2005] and Gillessen et al. [2009],respectively and parameters for DSO/G2 were obtained from Valencia-S. et al. [2015] and they were used for further analysis of bow-shock shells. The distances and the velocities at the apocentre and at the pericentre were computed from eq. (3.1), (3.2) and (3.5). The errors were computed by the relation for the propagation of uncertainty. These values were also compared to values computed by program in Appendix A and the analytically obtained values vary from numerically computed values less than 1%.

In Fig. 3.3 we express the importance of the velocity of the star with respect to the ambient medium. If the star moves subsonically, bow-shock structures are not formed. Similar graph can be reproduced for any star so we can find out whether these structures are about to happen. In general, it needs to be stressed out that the velocities are highly dependent on the temperature and the density profiles of the ambient medium. In our model we assume that the central cavity is filled with ionized hot and sparse gas mostly made by massive stars near the Galactic centre. The number density and temperature profiles are then given by

$$n_{\mathrm{a}} \approx n_{\mathrm{a0}} \left(\frac{r_{\mathrm{s}}}{r}\right) \ , \tag{3.6}$$

$$T_{\mathrm{a}} \approx T_{\mathrm{a0}} \left(\frac{r_{\mathrm{s}}}{r}\right) \ , \tag{3.7}$$

where r is the distance from the SMBH Sgr A* and r_{s} is the Schwarzschild radius (for Sgr A* is r_{s} approximately $2.95{\times}10^5\ M_\bullet/M_\odot$ cm). The normalization parameters ($n_{\mathrm{a0}} = 1.3 \times 10^7 \mathrm{cm}^{-3}$ and $T_{\mathrm{a0}} = 9.5 \times 10^{10}\mathrm{K}$) are obtained from fitting these profiles by semi-analytical radial profiles based on the model of radially inefficient time-dependent accretion flows. For more see Blandford and Begelman [1999], Broderick and Loeb [2006] and Broderick et al. [2011]. It was

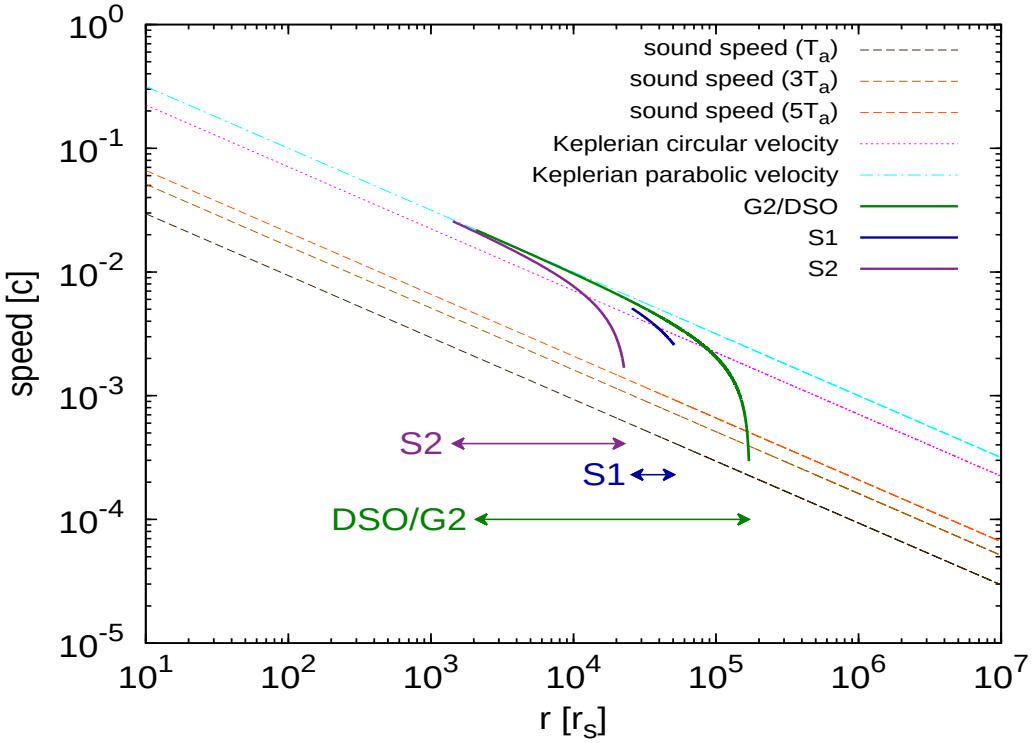

Figure 3.3. Comparison of Keplerian circular (neon green dashed line), parabolic (pink dashed lineline) and elliptic velocities (solid lines) of sources S1,S2 and DSO/G2 with speed of sound in central cavity (black, light brown and red dashed lines). All mentioned velocities are plotted as a function of distance r from the SMBH. Three lines for speed of sound vary through different temperatures of electron and ion components. All objects (S1, S2 and DSO/G2) are labelled with arrows, whose range is between r_{apo} and r_{peri} from table 3.2.

proven through the three-dimensional general relativistic magneto-hydrodynamic (GRMHD) simulations performed to millimetre observations of Sgr A* that the

ion temperature can be 1–5 times higher then the electron temperature [Dexter et al., 2010]. This is shown by three lines in Fig. 3.3 for the sound speed. Keplerian circular and parabolic velocities in the graph are given by eq. (3.3) and eq. (3.4), respectively. Elliptical velocities are plotted as a function of $r \in (r_{\mathrm{per}}, r_{\mathrm{apo}})$ following the eq. (3.5).

If the ideal gas is assumed, we obtain a formula for the sound speed as $c_{\mathrm{s}} = \sqrt{\frac{k_{\mathrm{B}} T_{\mathrm{a}}}{\mu m_{\mathrm{H}}}}$ from eq. (3.6) and eq. (3.7) [Zajaček et al., 2016]. Circular and parabolic velocities are approximately one order from the sound speed in the central cavity. The parabolic velocity is higher then the circular velocity. The velocities of stars S1 and S2 are also higher in comparison with the assumed profile of sound speed. The velocity of the object DSO/G2 is mostly above lines for the sound speed but this can be disputable when it approaches the pericentre. At the pericentre it moves supersonically for the cases of the temperature $3T_{\mathrm{a}}$ and $5T_{\mathrm{a}}$, but in the case of the temperature T_{a} the object moves subsonically.

In recent years, the bow-shock structures have been found in different fields around Sgr A*. For an illustration, we chose some of the sources for which observations were performed. The brief summary of these results is in Tab. 3.3.

source	$\mathbf{R_0}$ **[au]**
X7	168
IRS 10W	525
IRS 5	575
IRS 1W	651
X3	1007
IRS 8	2349

Table 3.3. The observed standoff distances for different sources in the Galactic centre. Values for sources X7, X3 were obtained from Mužić et al. [2010], values for IRS 8 from Rauch et al. [2013] and values for IRS 5, IRS 1W and IRS 10W from Sanchez-Bermudez et al. [2014].

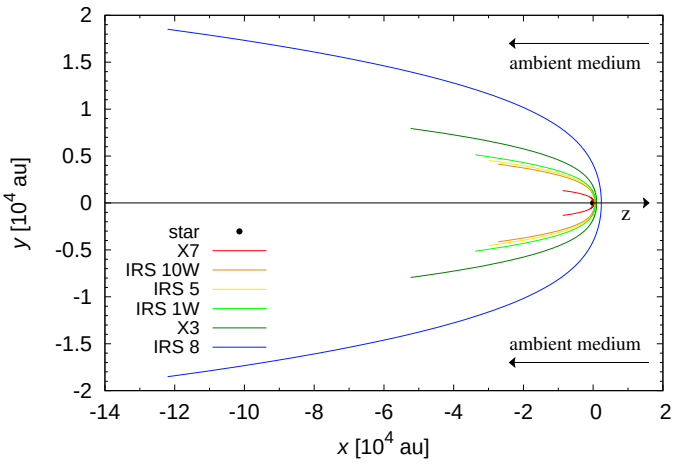

Figure 3.4. A graphical representation of the shape of bow shocks in a cross-section with the orbital plane for observed standoff distances from Tab. 3.3. Each line represents a different source. All the sources are set to the coordinate origin.

Mužić et al. [2010] and Rauch et al. [2013] developed bow-shock models for fitting observed data, and in their approach these constant standoff distances were obtained as best fit results from models.

In Fig. 3.4 we show the bow-shock shells for these six sources. We put all of the stars to the same coordinate origin. Obviously, the parameter R_0 is the scaling parameter for the bow-shock shells. With the increase of R_0, the shell becomes bigger and more open.

Bow-shock shells can be variously sized by changing the parameters in eq. (2.7). Four parameters can be changed in eq. (2.7) and those are: the velocity of wind of the star $V_{\rm w}$, the mass-loss rate $\dot{m}_{\rm w}$, the relative velocity of the star with respect to the ambient medium $V^{\star}$ and the density of the ambient medium $\rho_{\rm A}$. According to Valencia-S. et al. [2015], where observations of the emission of

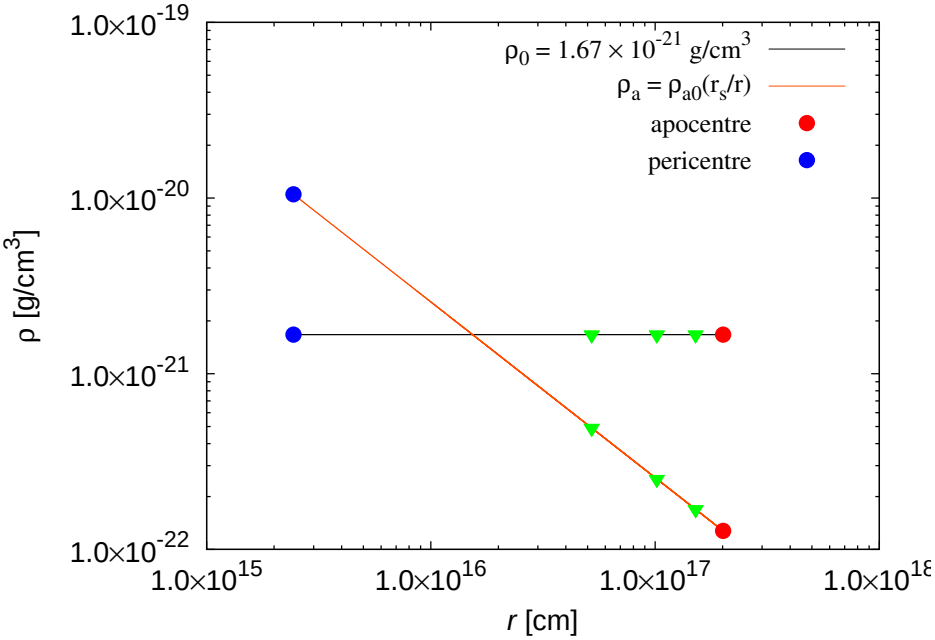

Figure 3.5. Behaviour of radial density $\rho_{\rm a}$ (orange line) in comparison with the constant value of the density ρ_0 (black line). Marked points refer to the same points we chose for plotting bow-shock shells along the orbit of the fiducial S-star (Fig. 3.7, 3.8, 3.9 and 3.10) except the zoomed in picture (Fig. 3.11).

DSO/G2 were compared with the model of a pre-main sequence star, we set up the mass-loss rate of our fiducial S-star to $10^{-8} M_{\odot}{\rm yr}^{-1}$. For a model that considers the mass-loss envelope of a young T Tauri star, see Scoville and Burkert [2013]. For the density $\rho_{\rm A}$ from eq. (2.7) we considered two values: the constant density $\rho_0 = 1.67 \times 10^{-21}{\rm g/cm}^3$ and the density $\rho_{\rm a}$ decreasing as $\sim 1/r$, where r stands for the distance from Sgr A* (for more about behaviour of the densities, see Fig. 3.5). In the case of the constant density, we considered the number density as 10^3 particles for one cm^3 [Kunneriath et al., 2012]. The model for the decreasing density as $\sim 1/r$ is from the eq. (3.6). The velocity of a stellar wind was set to 20, 200 and 2000 km/s. For more details about mass-loss rates and stellar winds see Naiman et al. [2013], Voss et al. [2009] or Puls et al. [2008]. For all graphs we chose eight points, where the bow-shock shells were plotted. Those points were approximately 5000 au away from each other (measured on x-axis).

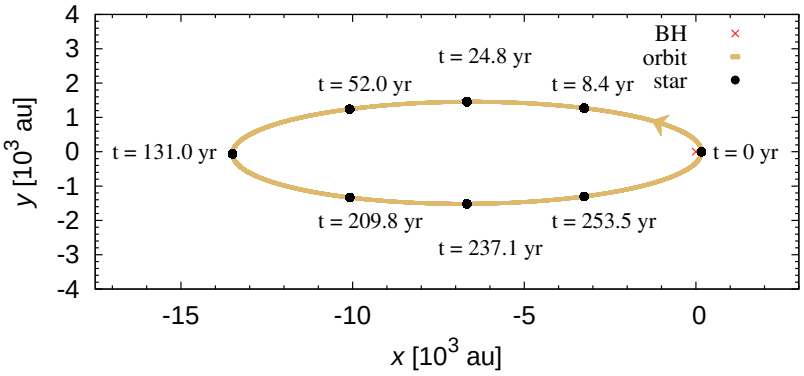

Figure 3.6. The orbit of the fiducial S-star. Marked points refer to points in which we plotted bow-shock shells in Sec. 3.2

In Sec. 3.4 we will refer to these points as points labelled in some exact time (Fig. 3.6).

3.2 Bow-shock shell along the orbit

Assuming the ambient medium near the SMBH at rest, the relative velocity of the star with respect to the ambient medium is identical with the orbital velocity of the star (Fig. 3.7). The changing parameter in the pictures of Fig. 3.7 is the value of the stellar wind V_{w}. If the value of V_{w} is bigger, the bow-shock shell is larger and more open. We need to mention that for plotting purposes, the length of a bow-shock tail is not always the same. We changed that parameter for getting more illustrative picture, but usually the change was only in the case of the maximum bow-shock shell, especially when $V_{\mathrm{w}} = 2000$ km/s. The bow-shock tail was so long that the actual size of the orbit was too small for a good recognition of other plotted shells. The inclination angle of bow-shock shells is set to 90°.

If there is a radial outflow from the SMBH (Fig. 3.8) or an inflow onto the SMBH (Fig. 3.9), the final velocity vector is a relative vector of the star with respect to the ambient medium. The same analysis is applied in the case of the combined model of an outflow and an inflow (Fig. 3.10). The velocity of the stellar wind is set to $V_{\mathrm{w}} = 200$ km/s. Parameter V_0 represents the velocity of the ambient medium. Parameter r_{B} is the so-called Bondi radius (in Fig. 3.10 marked with the light purple circle), which represents the border between the outflow and the inflow (see Sec. 2.1 and eq. (2.21)). At the border we consider $V_0 = 0$ km/s. The Bondi radius is set to ≈ 33000 au for our Galaxy (see Sec. 2.1), though, for a demonstrative purpose of the combined model of the fiducial S-star orbit we set this parameter to 8000 au. But based on Wang et al. [2013] we should consider the inflow model (Fig. 2.2) for the whole orbit of the fiducial S-star for the temperature of $T_{\mathrm{a}} = 10^7$K (for more details see the beginning of Sec. 3.1). The inclination angle of the bow-shock shell is set to 90°(it is valid for graphs 3.8, 3.9 and 3.10).

On the other hand, the Bondi radius set to 8000 au does not need to be only a hypothetical scenario. We can derive a relation for the Bondi radius only as a

function of the temperature T_a of the ambient medium (ideal gas) as

$$r_\mathrm{B} = \frac{GM_\bullet}{{c_\mathrm{s}}^2} = \frac{GM_\bullet \mu m_\mathrm{H}}{k_\mathrm{B}} (T_\mathrm{a})^{-1} = 4'' \left(\frac{M_\bullet}{4 \times 10^6 M_\odot} \right) \left(\frac{T_\mathrm{a}}{10^7 \mathrm{K}} \right)^{-1} , \qquad (3.8)$$

which means that the temperature needs to be only approximately four times higher than 10^7K if we want to get $r_\mathrm{B} = 8000$ au. This relation also gives the numerical estimation of the Bondi radius. This increase of the temperature could possibly happen at time when our Galactic centre was active.

For each case of zero velocity of the ambient medium, radial outflow and radial inflow was made a graph of zoomed in area near the SMBH, where the star passes through the pericentre (Fig. 3.11). The inclination angle of the bow-shock shell is again set to 90°.

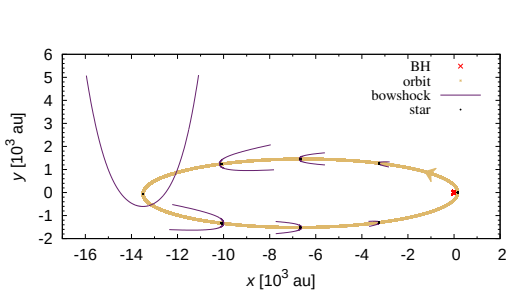

(a) $\rho_\mathrm{a} = \rho_{\mathrm{a}0}(r_\mathrm{s}/r)$, $V_\mathrm{w} = 20$ km/s

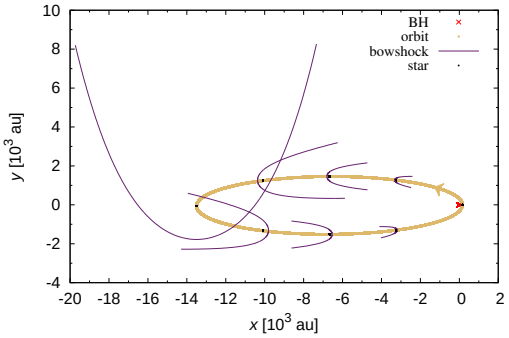

(b) $\rho_\mathrm{a} = \rho_{\mathrm{a}0}(r_\mathrm{s}/r)$, $V_\mathrm{w} = 200$ km/s

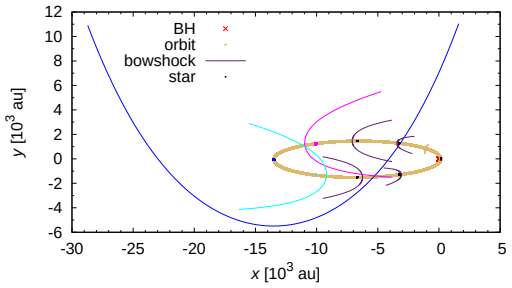

(c) $\rho_\mathrm{a} = \rho_{\mathrm{a}0}(r_\mathrm{s}/r)$, $V_\mathrm{w} = 2000$ km/s

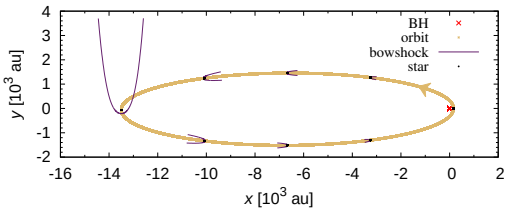

(d) $\rho_0 = 1.67 \times 10^{-21}$ g/cm^3 , $V_\mathrm{w} = 20$ km/s

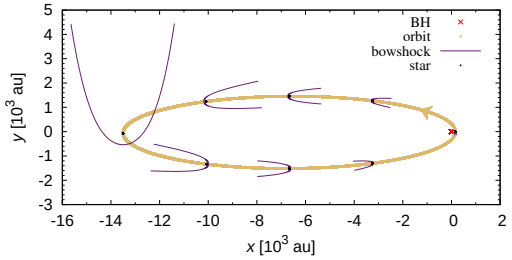

(e) $\rho_0 = 1.67 \times 10^{-21}$ g/cm^3 , $V_\mathrm{w} = 200$ km/s

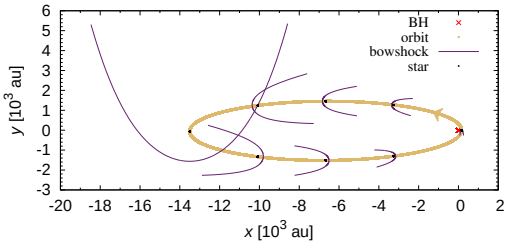

(f) $\rho_0 = 1.67 \times 10^{-21}$ g/cm^3 , $V_\mathrm{w} = 2000$ km/s

Figure 3.7. A graphical representation of the shape of bow shocks in a cross-section with the orbital plane. The bow-shock shells are shown along the orbit for the case of zero velocity of the ambient medium near the SMBH. Graphs vary by the density profile of the ambient medium and the value of the stellar wind V_w.

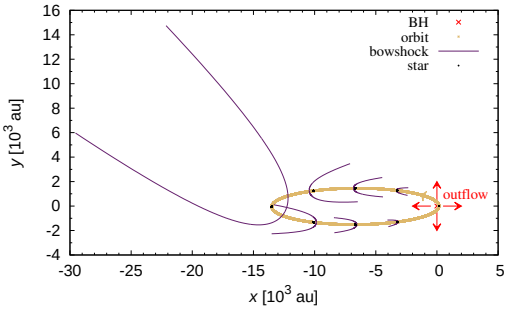

(a) $\rho_{\rm a} = \rho_{\rm a0}(r_{\rm s}/r)$, $V_0 = 100$ km/s

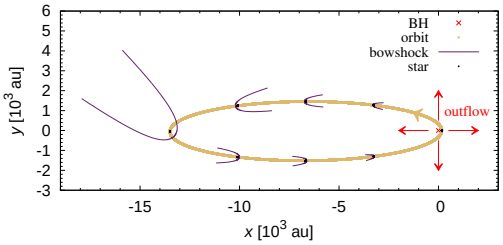

(b) $\rho_0 = 1.67 \times 10^{-21}$ g/cm^3, $V_0 = 100$ km/s

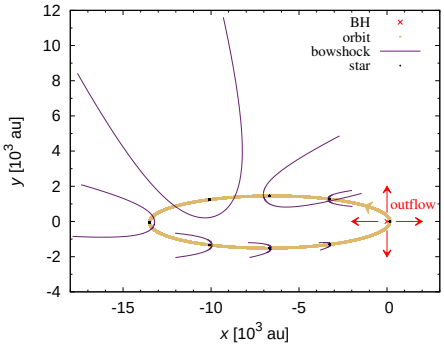

(c) $\rho_{\rm a} = \rho_{\rm a0}(r_{\rm s}/r)$, $V_0 = 500$ km/s

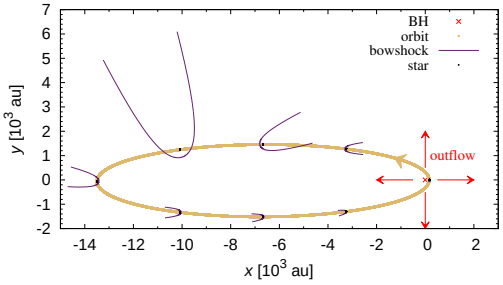

(d) $\rho_0 = 1.67 \times 10^{-21}$ g/cm^3, $V_0 = 500$ km/s

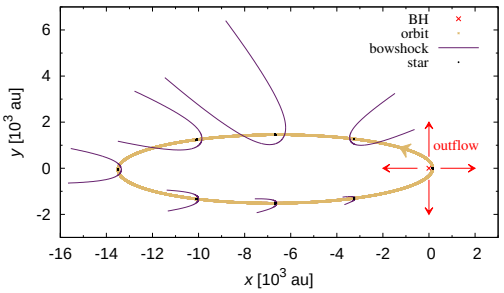

(e) $\rho_{\rm a} = \rho_{\rm a0}(r_{\rm s}/r)$, $V_0 = 1000$ km/s

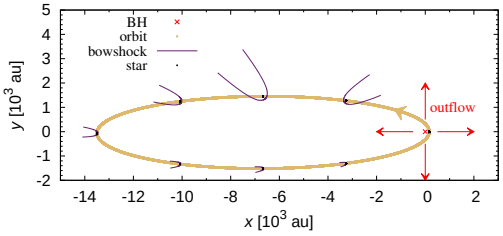

(f) $\rho_0 = 1.67 \times 10^{-21}$ g/cm^3, $V_0 = 1000$ km/s

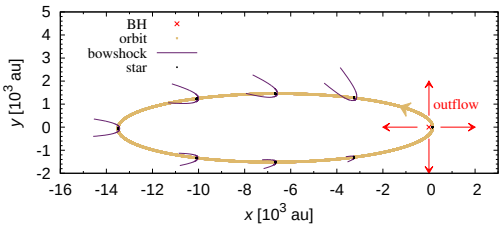

(g) $\rho_{\rm a} = \rho_{\rm a0}(r_{\rm s}/r)$, $V_0 = 2000$ km/s

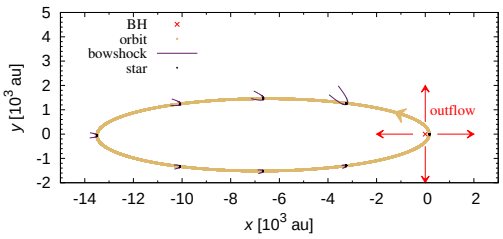

(h) $\rho_0 = 1.67 \times 10^{-21}$ g/cm^3, $V_0 = 2000$ km/s

Figure 3.8. A graphical representation of the shape and the orientation of bow shocks in a cross-section with the orbital plane. The bow-shock shells are shown along the orbit for the case of an outflow from the SMBH. Graphs vary by the density profile and by the velocity of the outflow V_0, which was set to (100, 500, 1000 or 2000) km/s. The parameter of the stellar wind $V_{\rm w}$ is fixed to 200 km/s.

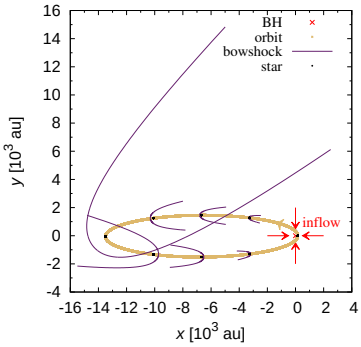

(a) $\rho_{\rm a} = \rho_{\rm a0}(r_{\rm s}/r)$, $V_0 = 100$ km/s

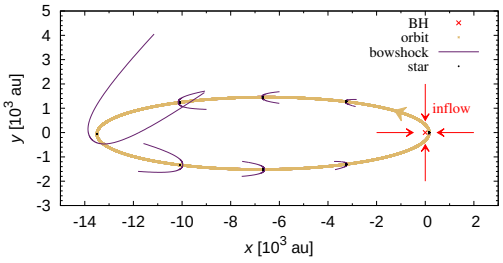

(b) $\rho_0 = 1.67 \times 10^{-21}$ g/cm^3, $V_0 = 100$ km/s

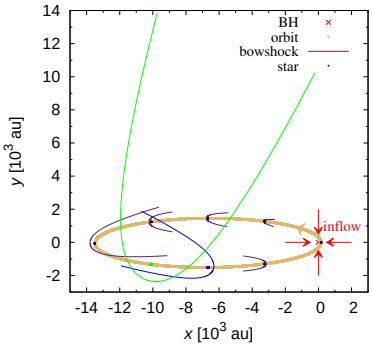

(c) $\rho_{\rm a} = \rho_{\rm a0}(r_{\rm s}/r)$, $V_0 = 500$ km/s

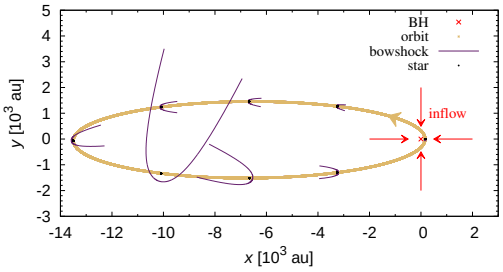

(d) $\rho_0 = 1.67 \times 10^{-21}$ g/cm^3, $V_0 = 500$ km/s

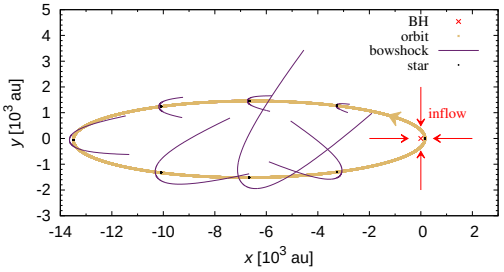

(e) $\rho_{\rm a} = \rho_{\rm a0}(r_{\rm s}/r)$, $V_0 = 1000$ km/s

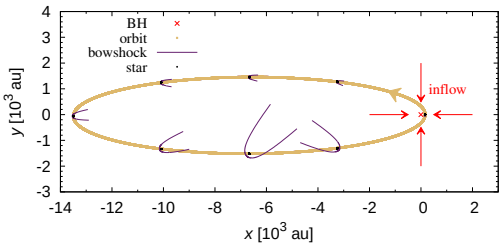

(f) $\rho_0 = 1.67 \times 10^{-21}$ g/cm^3, $V_0 = 1000$ km/s

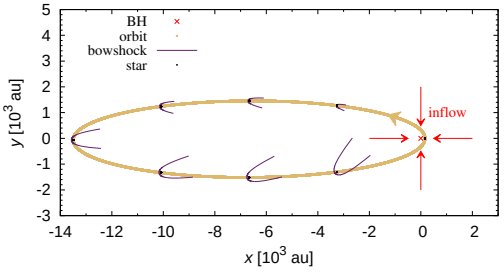

(g) $\rho_{\rm a} = \rho_{\rm a0}(r_{\rm s}/r)$, $V_0 = 2000$ km/s

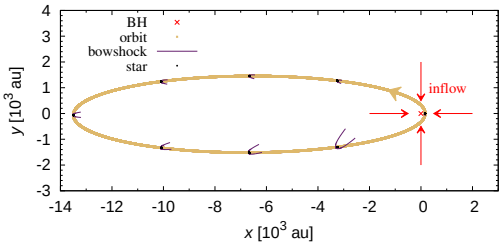

(h) $\rho_0 = 1.67 \times 10^{-21}$ g/cm^3, $V_0 = 2000$ km/s

Figure 3.9. The same as Fig. 3.8 but for an inflow onto the SMBH.

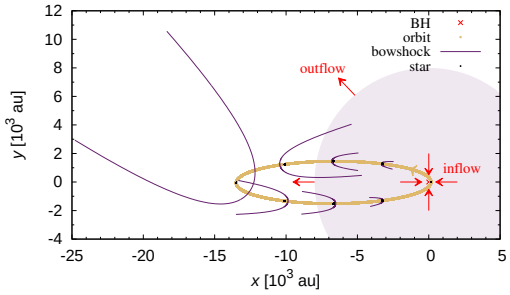

(a) $\rho_{\rm a} = \rho_{\rm a0}(r_{\rm s}/r)$, $V_0 = 100$ km/s

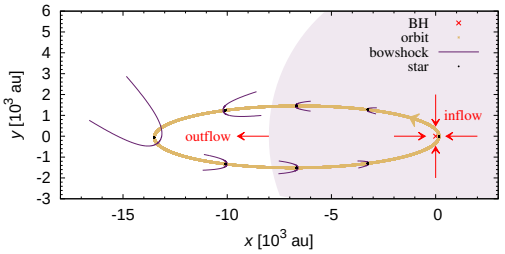

(b) $\rho_0 = 1.67 \times 10^{-21}$ g/cm^3, $V_0 = 100$ km/s

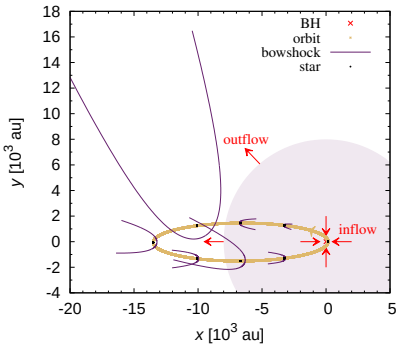

(c) $\rho_{\rm a} = \rho_{\rm a0}(r_{\rm s}/r)$, $V_0 = 500$ km/s

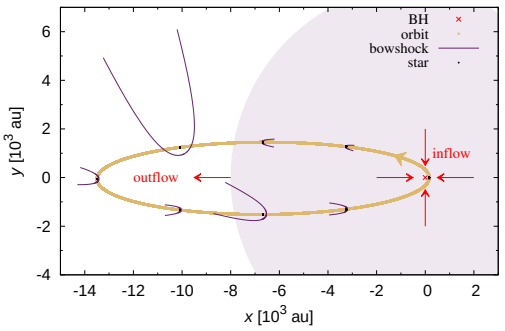

(d) $\rho_0 = 1.67 \times 10^{-21}$ g/cm^3, $V_0 = 500$ km/s

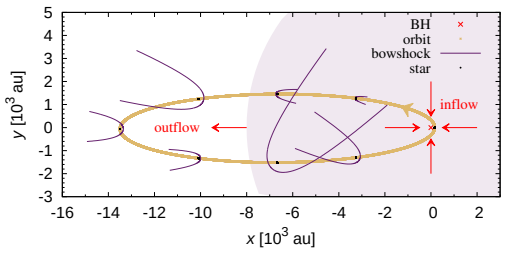

(e) $\rho_{\rm a} = \rho_{\rm a0}(r_{\rm s}/r)$, $V_0 = 1000$ km/s

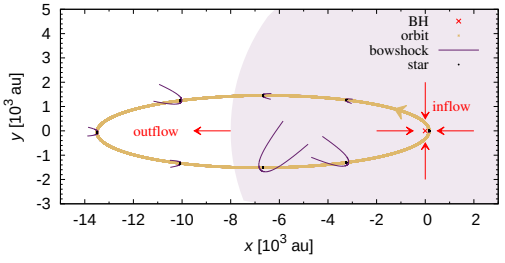

(f) $\rho_0 = 1.67 \times 10^{-21}$ g/cm^3, $V_0 = 1000$ km/s

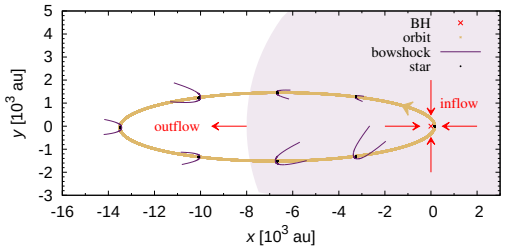

(g) $\rho_{\rm a} = \rho_{\rm a0}(r_{\rm s}/r)$, $V_0 = 2000$ km/s

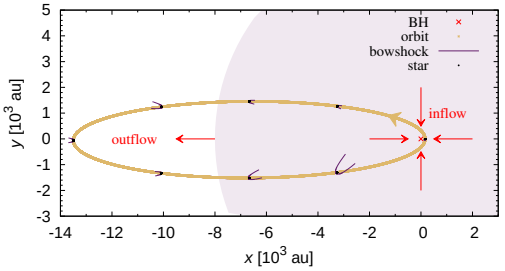

(h) $\rho_0 = 1.67 \times 10^{-21}$ g/cm^3, $V_0 = 2000$ km/s

Figure 3.10. The same as Fig. 3.8 but for the combined model of an outflow from the SMBH and an inflow onto the SMBH. Light purple circle with the radius $r_{\rm B} = 8000$ au marks the area between the inflow and the outflow.

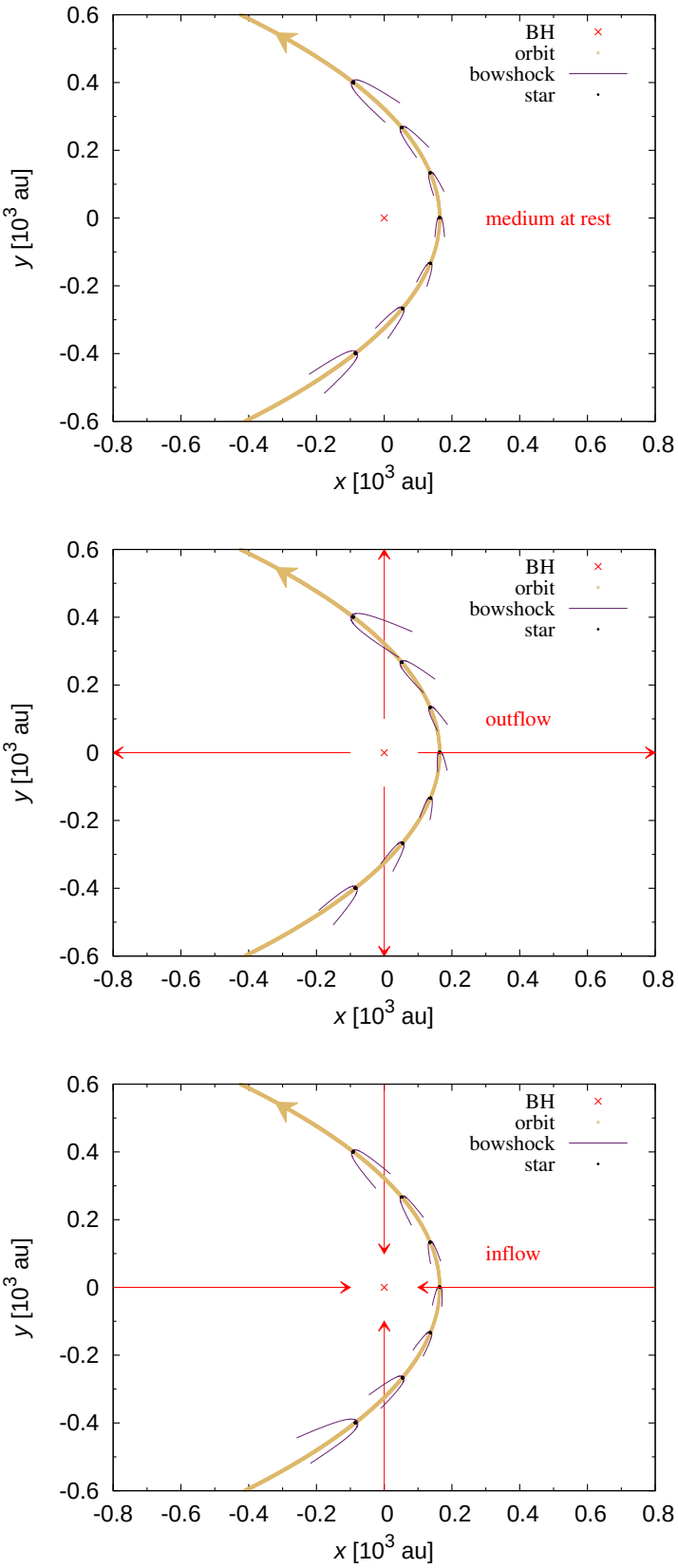

Figure 3.11. Zoomed-in area near the SMBH entered from the Fig. 3.7(b) for the ambient medium at rest, Fig. 3.8(e) for the radial outflow from the SMBH and Fig. 3.9(e) for the radial inflow onto the SMBH. For all graphs we used $\rho_{\rm a} = \rho_{\rm a0}(r_{\rm s}/r)$, $V_{\rm w} = 200$ km/s and $V_0 = 1000$ km/s. *Top panel*: The model for the zero velocity of the ambient medium. *Middle panel*: The radial outflow model. *Bottom panel*: The radial inflow model.

3.3 Standoff distance and star velocity

We plotted following graphs for one orbit of the fiducial S-star (period of one orbit is $T = 262$ years, see also Tab. 3.2), where we set the parameter of the wind velocity to 200 km/s and we considered the radially decreasing density profile (for the comparison of radially decreasing density profile and the constant density profile see Fig. 3.12).

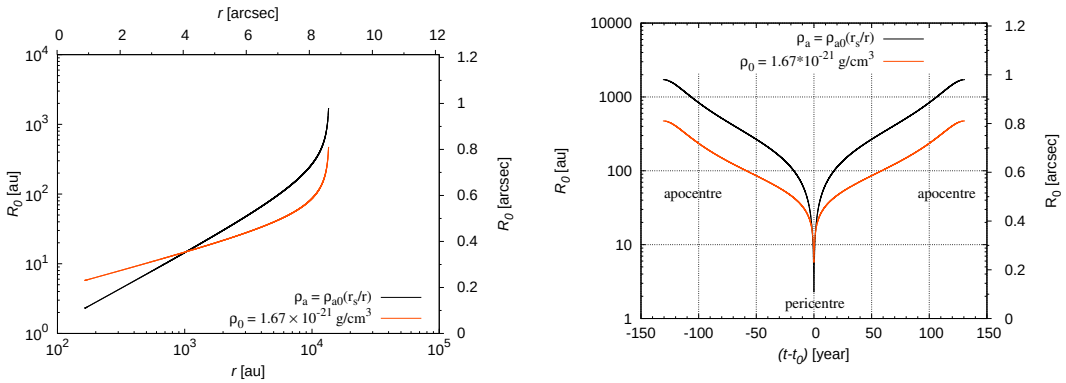

Figure 3.12. Dependence of the standoff distance on the distance from the SMBH (left panel) and on time (right panel). The constant parameter of t_0 is set to 131 years and it is the moment when the star passes through the apocentre. The black line represents the profile for the radially decreasing density and the red line represents the constant density profile. In comparison with the radially decreasing density profile, the constant density profile has lower standoff distance values. These profiles were performed for the model considering the ambient medium at rest and for $V_{\mathrm{w}} = 200$ km/s.

Figures 3.13 and 3.14 show that even if the outflow from the Galactic centre is symmetric and the stellar wind is considered to be isotropic, the behaviour of the star – Sgr A* system appears to be asymmetric along the orbit of the star [Zajaček et al., 2016].

For the ambient medium at rest (represented by the black line in following figures), the maximum standoff distance is at the apocentre (≈ 1700 au) and the minimum occurs to be at the pericentre (≈ 2 au). With the increasing radial outflow V_0, the minimum stays the same but the maximum of R_0 is decreasing and moving towards the pericentre. This is clearly seen in Fig. 3.13 (graphs R_0 vs. r and R_0 vs. $(t - t_0)$). Parameter t_0 stands for the moment of the apocentre passage. In Fig. 3.13 there is a clear evidence that the maximum of R_0 occurs after the star passes through the pericentre.

The asymmetric behaviour is also seen in Fig. 3.14 for different profiles of the outflow velocity. With zero velocity of the outflow, the velocity of the star behaves symmetrically. The star passes through the pericentre with the highest velocity (≈ 7000 km/s) and its velocity reaches the minimum at the apocentre (≈ 90 km/s). With the increasing velocity of the outflow, the asymmetry between the post-pericentre and the pre-pericentre phase is significant. Both the maximum and the minimum of the star velocity increase towards the pericentre (left panel in Fig. 3.14). Considering non-zero radial outflow, the maximal velocity of the star is at the pericentre and its minimum occurs after the passage through the pericentre in the post-pericentre phase.

Previously discussed symmetries and asymmetries for the standoff distance

and for the velocity of the star, which in turn depend on the velocity of the outflow from Sgr A*, are very similar to ones considering the radial inflow onto the SMBH. The difference is in the exchange between the post-pericentre and the pre-pericentre values. For the ambient medium at rest, the behaviour of the standoff distance and velocity profiles is the same. With increasing velocity of the inflow, the maximum value of R_0 is again decreasing and moving towards the pericentre (top panel of Fig. 3.15). Its maximal value occurs to be in the pre-pericentre phase (bottom panel of Fig. 3.15). For non-zero radial inflow, the maximal velocity of the star is at the pericentre and the minimal star velocity is in the pre-pericentre phase (see Fig. 3.16).

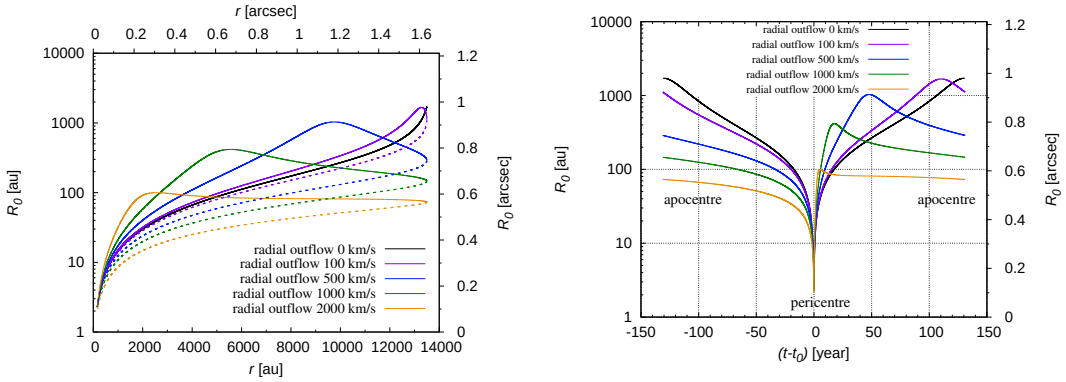

Figure 3.13. Dependence of the standoff distance R_0 on the distance r from the SMBH (left panel) and on the time interval $(t-t_0)$ (right panel) for the ambient medium at rest (black line) and for different velocities of the outflow from the SMBH (colour lines). Constant parameter of t_0 is set to 131 years and it stands for the moment when the star passes through the apocentre. Solid lines represent post-pericentre phase and dashed lines correspond to pre-pericentre phase. Another axis was added for values of r and R_0 in units of arcseconds, calculated for the distance Sgr A* – Earth.

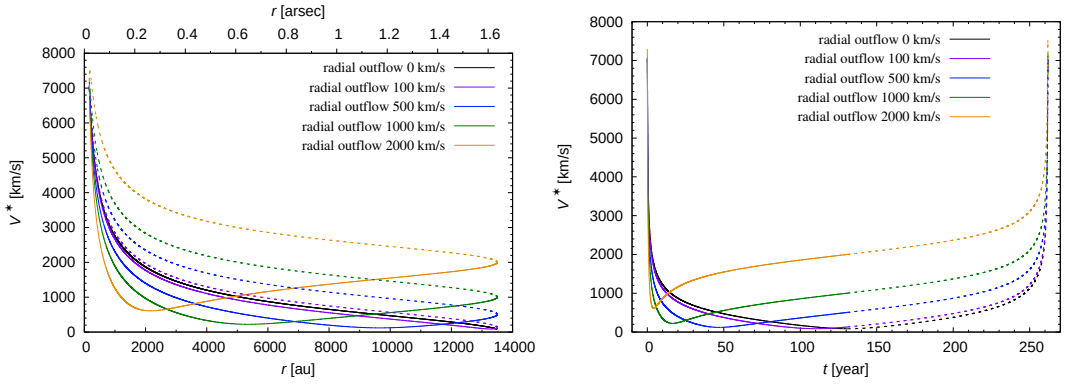

Figure 3.14. Dependence of the star velocity $V^\star$ on the distance r from the SMBH and time t for the ambient medium at rest (represented by the black line) and for different velocities of the outflow from the SMBH (represented by colour lines). Solid lines stand for the post-pericentre phase and dashed lines correspond to the pre-pericentre phase. Another axis was added for values of r in units of arcseconds, calculated for the distance Sgr A* – Earth.

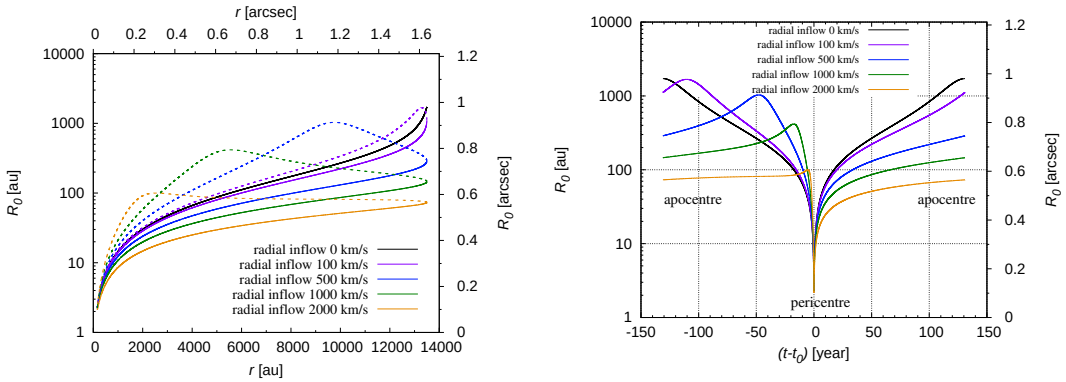

Figure 3.15. The same as Fig. 3.13 but for different velocities of the inflow onto the SMBH.

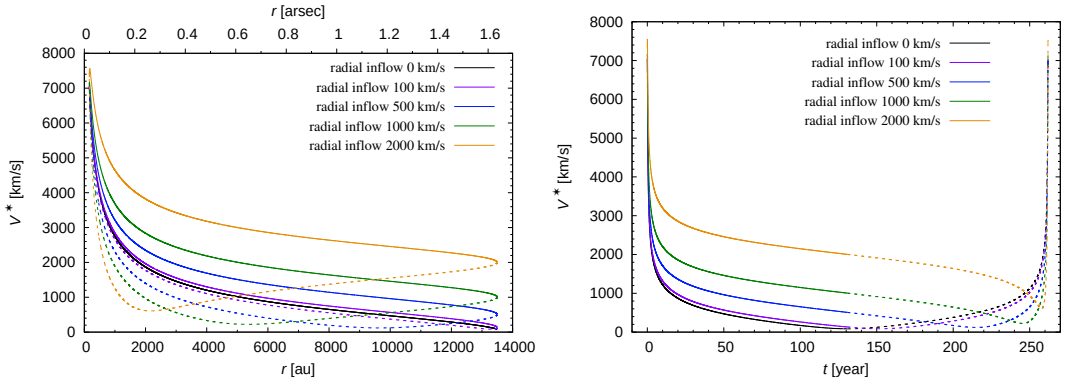

Figure 3.16. The same as Fig. 3.14 but for different velocities of the inflow onto the SMBH.

We plotted the same four graphs for the combined model (Fig. 3.18 and Fig. 3.19). The Bondi radius is set to $r_{\mathrm{B}} = 8000$ au. For $r < r_{\mathrm{B}}$ the graphs are identical with the ones for the inflow model, and for $r > r_{\mathrm{B}}$ the outflow prevails. The most interesting part occurs at the transition region, $r = r_{\mathrm{B}}$, where the medium is at rest. It needs to be stressed out that we adopted a simplified model. According to this scheme we assume that the density of the ambient medium does not affect the velocity of outflow/inflow, which is set to be constant ($100, 500, 1000$ or 2000 km/s). The cross-over between the inflow onto the SMBH and the outflow from the SMBH is not continuous at this point. When $r \longrightarrow r_{\mathrm{B}-}$, the value of the velocity V_0 is negative, while V_0 is positive if $r \longrightarrow r_{\mathrm{B}+}$. This lies behind the jump between the inflow and the outflow at the point $r = r_{\mathrm{B}}$.

The exact orientation for these plots is illustrated in Fig. 3.17. In our computations, at time $t = 0$, the star is at the pericentre – $r \approx 164$ au (according to Tab. 3.2) and one needs to follow the solid line arrows. Then at time of the passage through the apocentre ($t = 131$ years and $r \approx 13500$ au), dashed line arrows need to be followed. The increasing asymmetries of the combined model, in the comparison with the previous considered models, are obvious in Fig. 3.18 and Fig. 3.19.

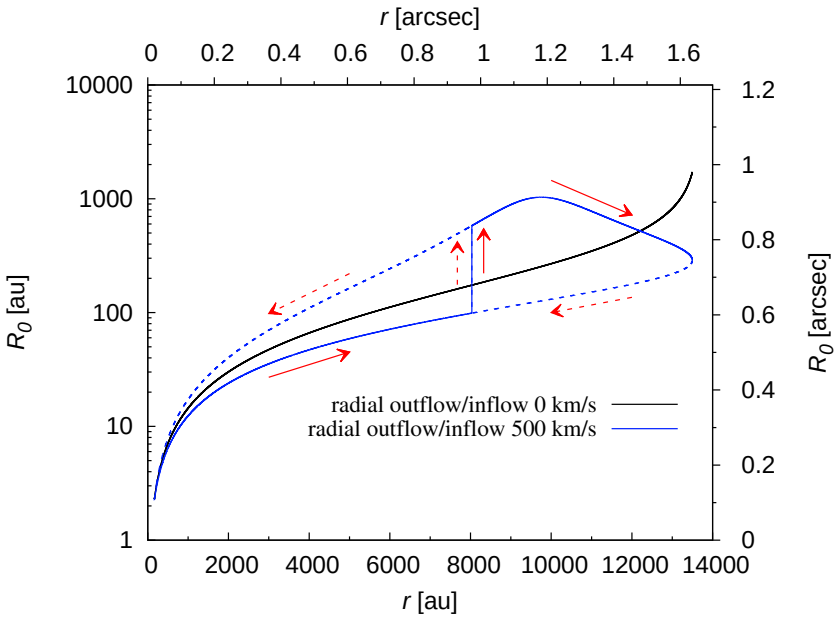

Figure 3.17. Dependence of the standoff distance R_0 of the bow-shock shells on the distance r from the SMBH. The velocity of the outflow/inflow is set to 0 km/s for the black line and 500 km/s for the blue line (the post-pericentre phase is represented by the blue solid line and the blue dashed line corresponds to the pre-pericentre phase). For further details and the values of other parameters see the main text.

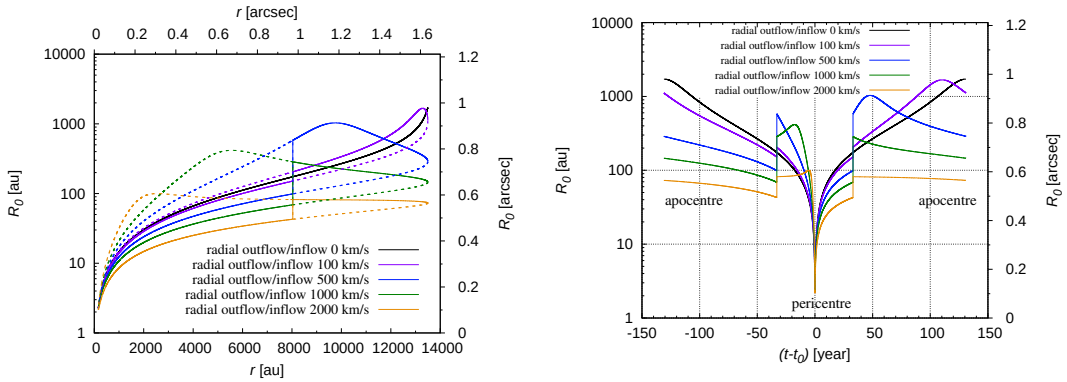

Figure 3.18. The same as Fig. 3.13 but for the combined model. The Bondi radius is set to 8000 au.

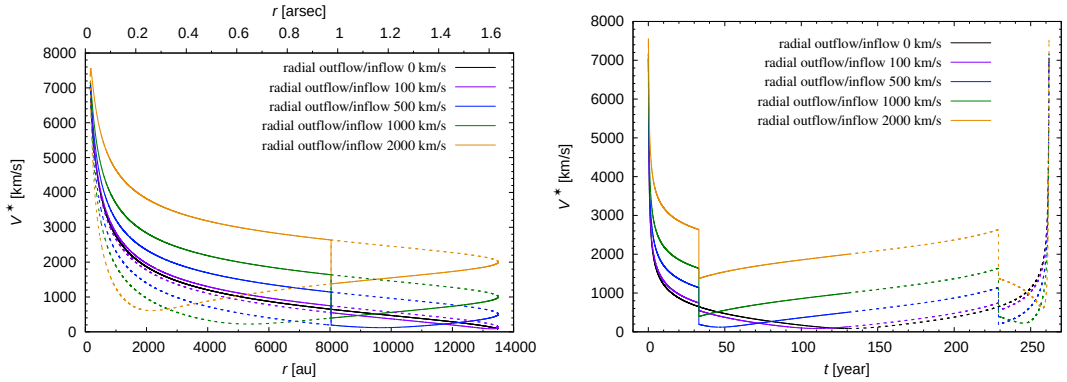

Figure 3.19. The same as Fig. 3.14 but for the combined model. The Bondi radius is set to 8000 au.

3.4 Tangential velocity and mass surface density

Equation (2.10) refers to the tangential velocity in the shell and eq. (2.9) represents the mass surface density of the shell. These dependences are plotted in Fig. 3.20 for different values of the parameter $\alpha \equiv V^\star/V_\mathrm{w}$. According to Wilkin [1996], the value α is expected to be small for the majority of systems.

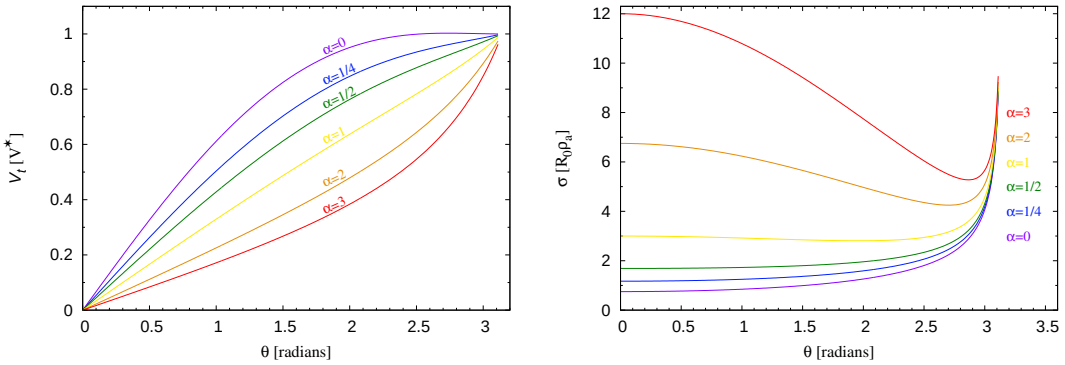

Figure 3.20. Profiles for the tangential velocity in the shell (left panel) and the mass surface density of the bow-shock shell (right panel) as a function of an angle θ for different values of $\alpha \equiv V^\star/V_\mathrm{w}$ (colour lines).

In our work we obtained also bigger values of α, compared to values in Fig. 3.20 from Wilkin [1996]. The main reason behind that is the location of our interest, which is set to the proximity of stars to the SMBH and thus large $V^\star$ with respect to V_w in the Galactic disc is obtained. It is obvious that the stars near

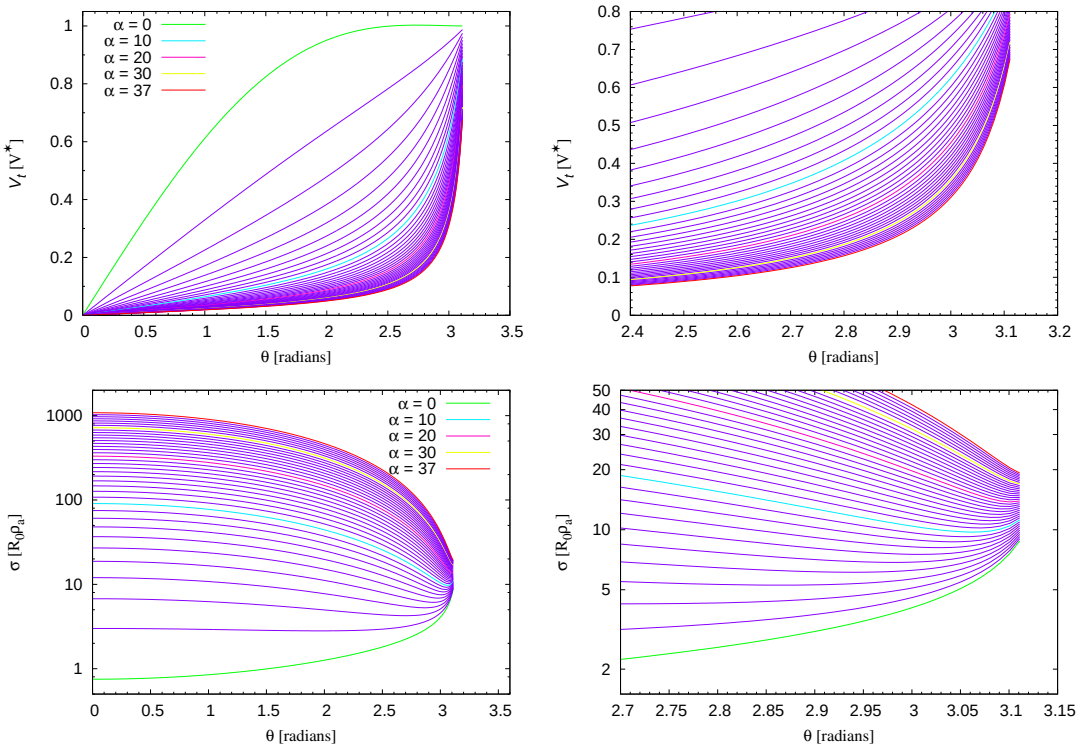

Figure 3.21. The same as 3.20 but for $\alpha \in (0, 1, 2, \ ..., \ 37)$. Right panels represent zoomed in areas of left panels. The legend in the left panel is also valid for the graph in the right panel.

the Galactic centre (especially at their pericentre) have higher velocities than stars located farther away from the central SMBH. Values of the parameter α in this work lie in the interval (0–37). Profiles of the tangential velocity and the mass surface density for this interval are plotted in 3.21.

In the following series of graphs, we computed the profiles for the velocity V_t and the mass surface density σ as a function of the spherical angle θ ($\theta \approx 0$ rad corresponds to the apex of the bow-shock shell and $\theta \approx 3.14$ rad corresponds to the end of the bow-shock tail) for different values of α, which were obtained for the inflow, the outflow or the combined models. Each parameter α in all of the graphs was calculated for the same positions, in which we plotted bow-shock shells in figures 3.7, 3.8, 3.9 and 3.10. We should mention that for time 0 years, the star is at the pericentre and in time 131 years star passes through the apocentre. The period of one orbit T is 262 years. All parameters of α were rounded to one decimal place, but they were computed with accuracy less than 1% (in fact, they were computed to 16 decimal places). Again the stellar wind is set to 200 km/s and the Bondi radius corresponds to 8000 au.

Values of α depend on the star velocity, which depends on the distance from the central SMBH. It is obvious that α varies rapidly with the consideration of various models for the medium at rest, the outflow, the inflow and the combined model with different velocities of outflow or inflow. For the model of the medium at rest, α values are same in the positions located at the same distance from the central SMBH (in Fig. 3.22 all lines for values of α overlap except those computed at the pericentre and the apocentre). The value of α is at the maximum at the

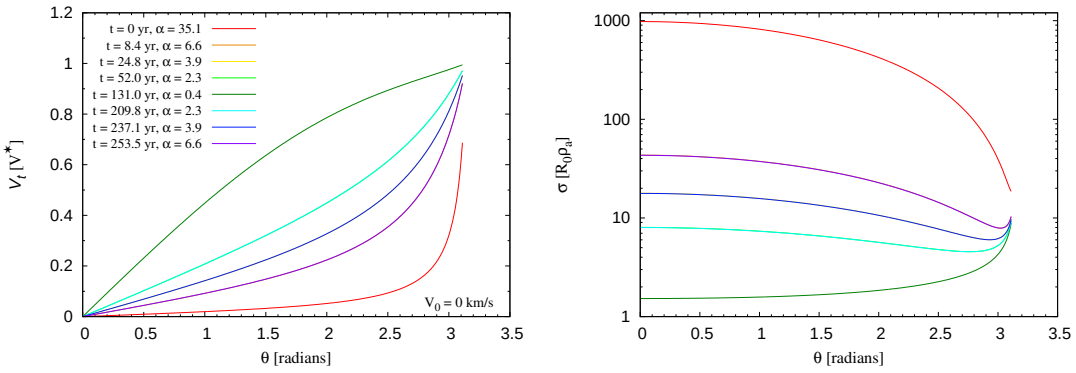

Figure 3.22. Profiles for the tangential velocity in the shell (left panel) and the mass surface density (right panel) of the bow-shock shell as a function of the angle θ for different values of $\alpha \equiv V^\star/V_\mathrm{w}$ (colour lines). The legend in the left panel is also valid for the right panel. For more details about the figures and parameters see the main text in this section (3.4).

pericentre and it is minimal at the apocentre. In fact, we could repeat the whole discussion for the α parameter from the subsection 3.3, specifically the discussion about the change of the velocity $V^\star$ along the orbit for different models. However, the shell velocity is negligible at the apex of the shell and it increases towards the bow-shock tail (see left panels of figures in subsections 3.4.1, 3.4.2 and 3.4.3). For all considered models of flows, increase of the velocity V_0 deepens the shell velocity profiles towards $\theta \approx 3.14$ rad. Vice versa, the mass surface density (see right panels of figures in subsections 3.4.1, 3.4.2 and 3.4.3) has a maximum at apex, it decreases towards the bow-shock tail and its minimal size is almost at the end of the tail.

For values of α smaller than ≈ 25, the profile of σ comes into its minimum for $\theta \approx$ 3 rad and then it slightly increases. On the other hand, for α around 30, the profile is decreasing along the whole bow-shock shell. Increasing outflow/inflow velocity causes that minimum of σ moves a little bit closer to $\theta = 3.14$ rad.

3.4.1 Outflow model

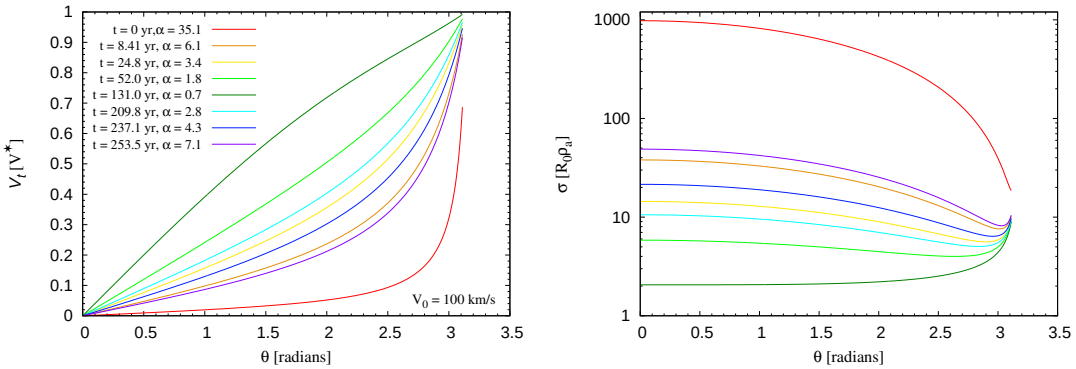

Figure 3.23. Profiles for the tangential velocity (left panel) and the mass surface density (right panel) in the shell as a function of the angle θ for different values of $\alpha \equiv V^\star/V_\mathrm{w}$ (colour lines). The velocity of the outflow from the SMBH is set to $V_0 = 100$ km/s and the velocity of the stellar wind is set to $V_\mathrm{w} = 200$ km/s. The legend in the left panel is also valid for the graph in the right panel.

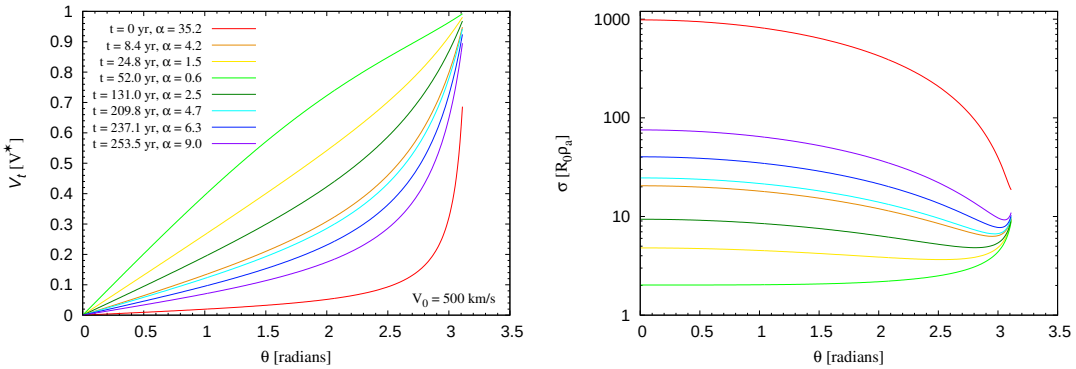

Figure 3.24. The same as Fig. 3.23 but the parameter V_0 is set to 500 km/s.

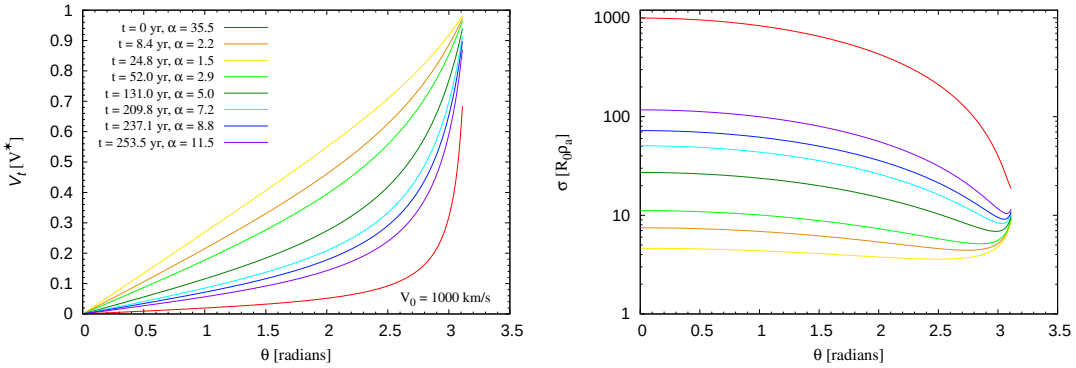

Figure 3.25. The same as Fig. 3.23 but the parameter V_0 is set to 1000 km/s.

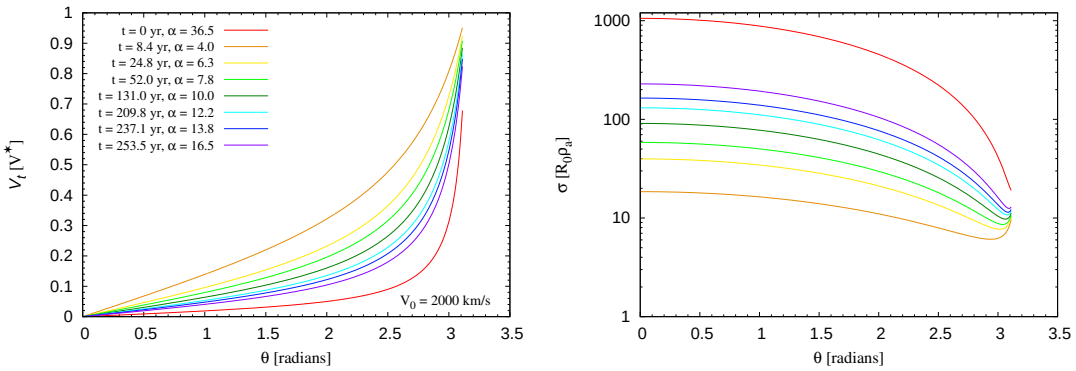

Figure 3.26. The same as Fig. 3.23 but the parameter V_0 is set to 2000 km/s.

3.4.2 Inflow model

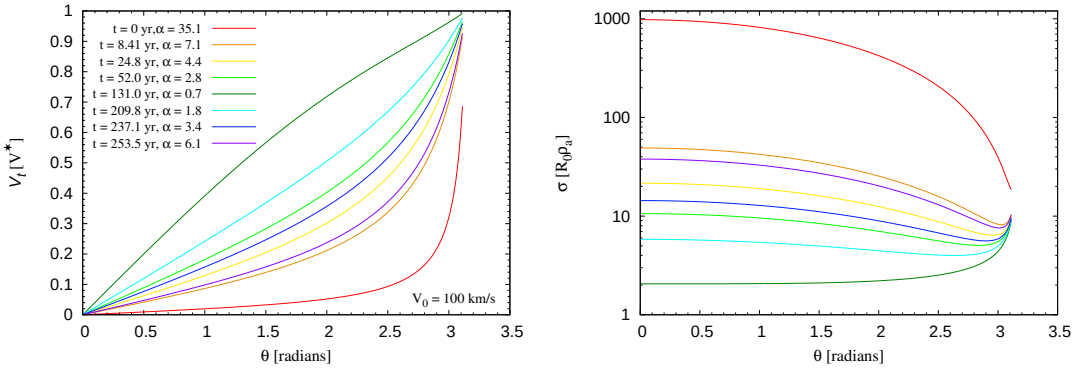

Figure 3.27. Profiles for the tangential velocity (left panel) and the mass surface density (right panel) in the shell as a function of the angle θ for different values of $\alpha \equiv V^\star/V_\mathrm{w}$ (colour lines). The velocity of the inflow onto the SMBH is set to $V_0 = 100$ km/s and the velocity of the stellar wind is set to $V_\mathrm{w} = 200$ km/s. The legend in the left panel is also valid for the graph in the right panel.

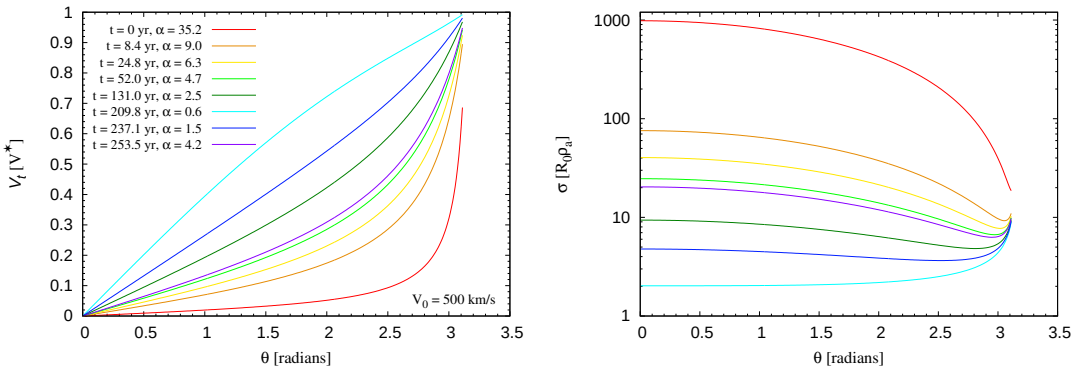

Figure 3.28. The same as Fig. 3.27 but the parameter V_0 is set to 500 km/s.

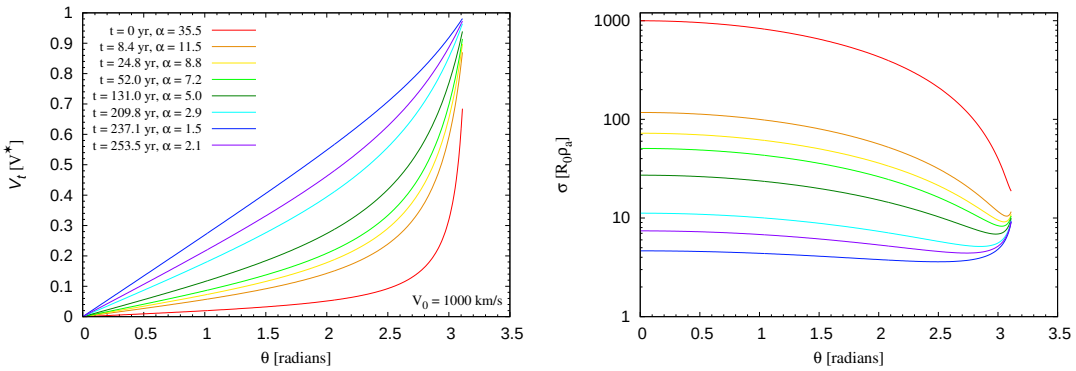

Figure 3.29. The same as Fig. 3.27 but the parameter V_0 is set to 1000 km/s.

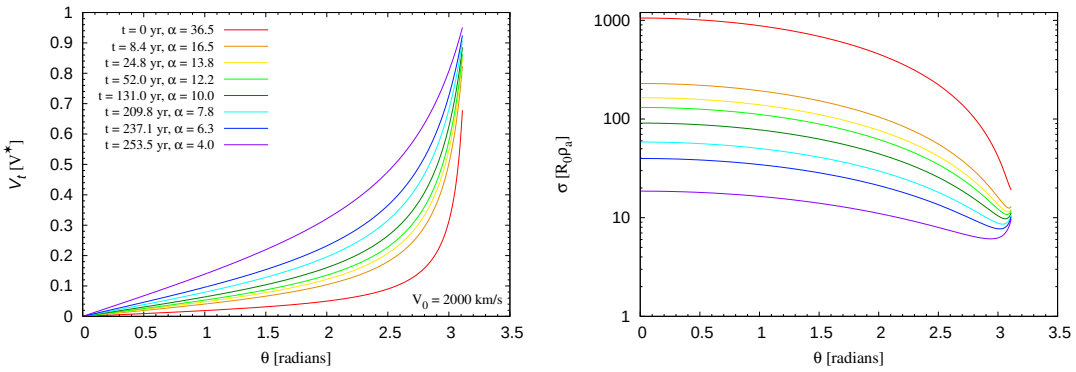

Figure 3.30. The same as Fig. 3.27 but the parameter V_0 is set to 2000 km/s.

3.4.3 Combined model

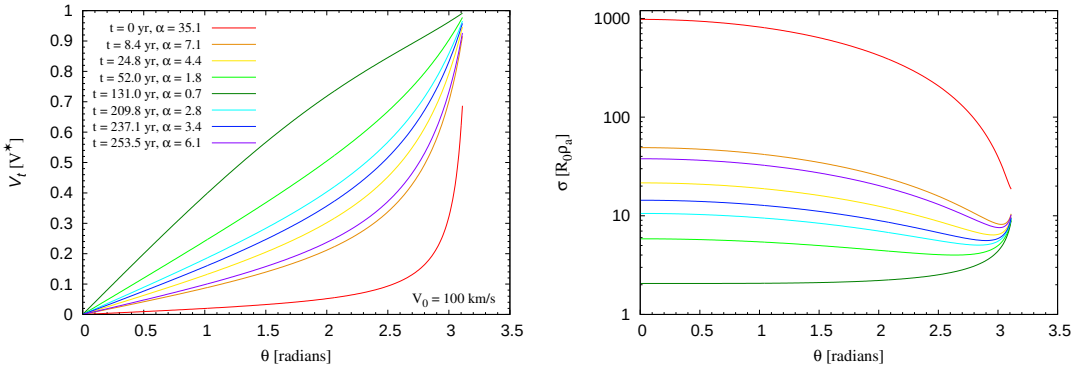

Figure 3.31. Profiles for the tangential velocity (left panel) and the mass surface density (right panel) in the shell as a function of the angle θ for different values of $\alpha \equiv V^\star/V_\mathrm{w}$ (colour lines). The velocity of the outflow from the SMBH and the inflow onto the SMBH is set to $V_0 = 100$ km/s and the velocity of the stellar wind is set to $V_\mathrm{w} = 200$ km/s. The Bondi radius is set to 8000 au. The legend in the left panel is also valid for the graph in the right panel.

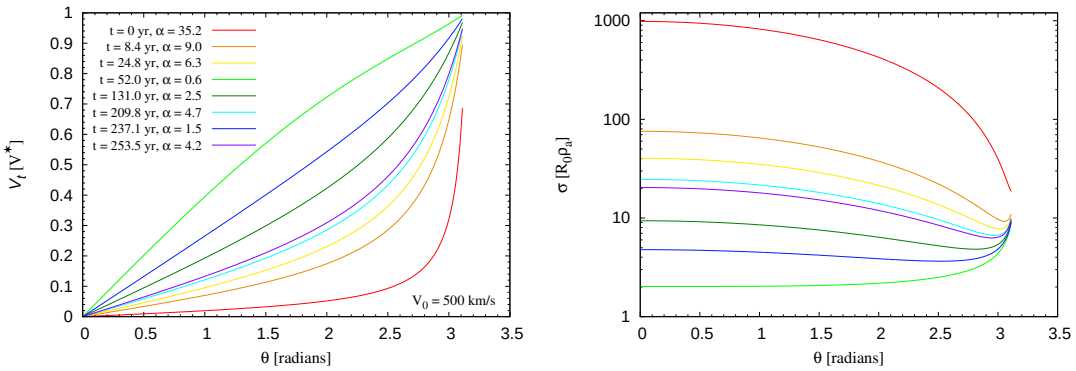

Figure 3.32. The same as Fig. 3.31 but the parameter V_0 is set to 500 km/s.

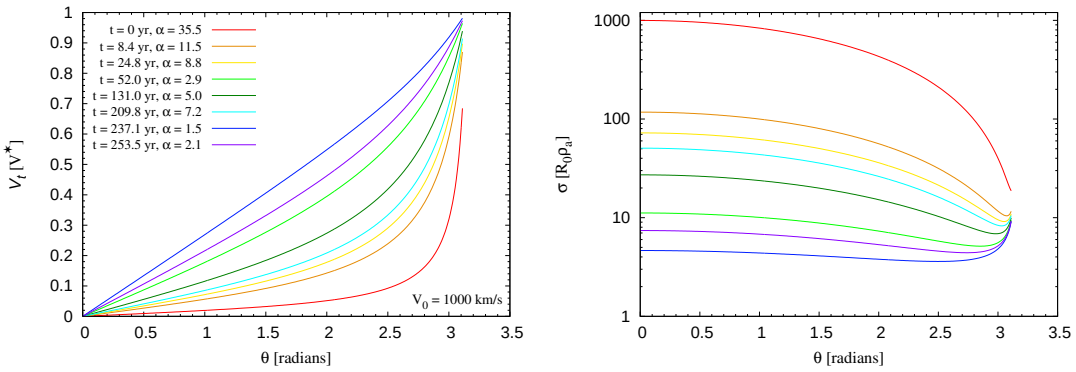

Figure 3.33. The same as Fig. 3.31 but the parameter V_0 is set to 1000 km/s.

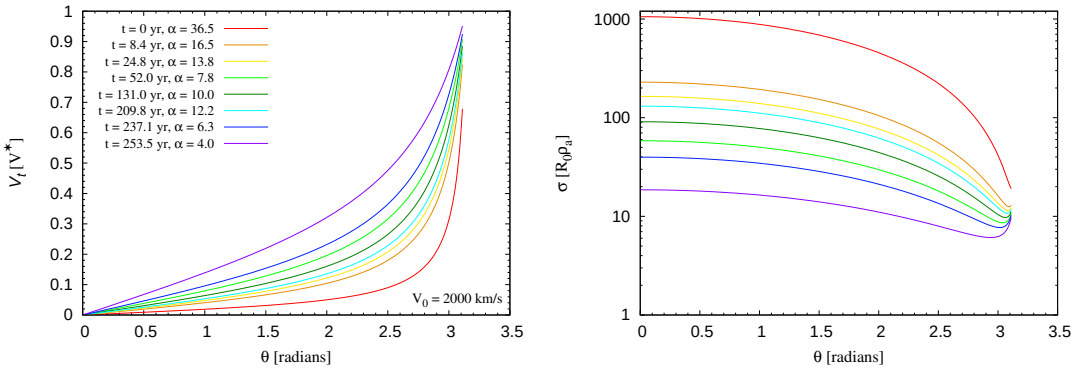

Figure 3.34. The same as Fig. 3.31 but the parameter V_0 is set to 1000 km/s.

4. Discussion

Comparing the standoff distances at the apocentre and at the pericentre we show the relation for the ratio of these distances only as a function of an eccentricity e and the power-law index γ. If the values e and γ increase, the ratio $\frac{R_{0\mathrm{Apo}}}{R_{0\mathrm{Peri}}}$ is bigger so the bow shock-shell at its apocentre is larger compared to the size of the shell at its pericentre. Once the values of the standoff distances are constrained from observations at the apocentre and at the pericentre together with the value of the eccentricity e, the value of γ can be found, and this way the exact power-law dependence for the density profile of the ambient medium can be determined near the Galactic centre. Next we derive the profile of the number density of the ambient medium in the hydrostatical equilibrium considering the Newtonian approximation. We obtain an exponential dependence on the distance r from the SMBH. Based on the observation of Wang et al. [2013], where the density of the ambient medium behaves as a decreasing function of the distance r we conclude that most probably the hydrostatic equilibrium does not occur near the Galactic centre.

We aim at the elliptic orbit of the fiducial S–star whose stellar velocity wind V_{w} is considered to be $(20, 200$ or $2000)$ km/s. All these possibilities for the stellar wind are discussed together with four models of flow near the SMBH: a model with zero velocity of an ambient medium, an outflow from the SMBH, an inflow onto the SMBH and a combined model considering an outflow and an inflow at the same time.

For the model with the ambient medium at rest we show, how bow-shock shells are affected by different velocities of the stellar wind V_{w}. For stars with the velocity of the stellar wind $V_{\mathrm{w}} = 20$ km/s, the bow-shock shell is smaller than the shell of stars whose stellar wind is set to $V_{\mathrm{w}} = 2000$ km/s. We also demonstrate the dependence of the size of shells on the density profile of the ambient medium. Bow-shock shells are smaller in the case of the constant density profile compared to the radially decreasing density profile. This model with zero velocity of the ambient medium is also specified by its symmetric behaviour for parameters R_0 (standoff distance) and $V^\star$ (relative velocity of the star with respect to the ambient medium) with respect to the passage through the pericentre.

Outflow, inflow and combined models are then discussed for the star whose velocity of the stellar wind is set to $V_{\mathrm{w}} = 200$ km/s. For these three models we consider four different velocities of flow from or onto the SMBH.

If we consider the outflow model, bow-shock shells take their maximal size after they pass through the pericentre but on the other hand, the shells for the inflow model are characterized by taking their maximal size before their pericentre passage. With increasing velocity of the outflow from and the inflow onto the SMBH, the maximal values of R_0 in both cases decrease and they shift towards the pericentre. The minimal values of R_0 decrease slightly in comparison with the maximal values in both models. If the outflow model is taken into account, the velocity of the star $V^\star$ decreases to its minimal value in the post-pericentre phase, and at the same phase it starts increasing until another post-pericentre phase. Increase of the velocity of the outflow causes that the minimal and also the maximal values of $V^\star$ increase and the minimum shifts towards the pericentre. The

same scenario is enacted in the case of the inflow model but the post-pericentre phase needs to be replaced by the pre-pericentre phase in the discussion above. The combined model shows the same characteristics as the inflow model below the Bondi radius and outside this radius it is characterised by the outflow model. The most interesting part occurs exactly at the Bondi radius, where the model is fully described by the model with zero velocity of the ambient medium. Compared to this model (the model for the medium at rest), these three models show asymmetric behaviour for parameters R_0 and $V^\star$ with respect to the pericentre passage. The combined model is the most asymmetric of them all.

We demonstrate the profiles for the tangential velocity in the shell and the mass surface density of the shell as a function of θ for different points along the orbit and for all of the previously mentioned models. These profiles show how the mass emanates along the shell of the bow-shock structure. The tangential velocity of the mass is trivial at the apex of the shell and it increases towards tails of the shell. The mass density profile has exactly the opposite behaviour. It is maximal at the apex of the bow-shock shell, then it decreases and almost at the end of the bow-shock shell it rapidly increases so the most of the shocked mass is located at the apex and also close to the end of the tail. But in terms of observations, this rapid increase of the mass near the tails of the shell is not usually observed. It is mainly because of the relatively high distance from the wind-blowing star. Both profiles for V_t and σ are strongly dependent on the value of $\alpha = V^\star/V_\mathrm{w}$. The tangential velocity profile deepens and lowers with the increasing parameter α. The mass surface density profile increases and creates the minimum almost at the end of the bow-shock tail at $\theta \approx 3$ rad. This minimum is present for almost all values of α and it slightly shifts towards the end of the tail. Now let us compare the changes of σ and V_t profiles for points along the orbit for different models. The increase of the velocity V_0 in each model causes that the V_t profiles lower and deepen. The σ profiles increase with increasing velocity V_0. If we assume the same velocities V_0 but different models, the profiles have the same behaviour and they vary through the parameter α, which is dependent on the star velocity $V^\star$.

All of our results are considered in the Newtonian approximation. Fig. 3.3 clearly shows that the neglect of relativistic effects was justified. The fiducial S-star, which is in details studied in this work, is located approximately 1000 Schwarzschild radii away from the SMBH. It is obvious that the relativistic effects are present here, but at this distance we are allowed to neglect them.

Although the calculations in this thesis are performed for specific parameters $\dot{m}_\mathrm{w}$, V_w, $V^\star$ and ρ_A from eq. (2.7), the results for different values of these parameters should change only quantitatively and not qualitatively. The parameter $\dot{m}_\mathrm{w}$ is set to $10^{-8} M_\odot \mathrm{yr}^{-1}$ in each calculation, but in general, it changes with the stellar type which is also related to the velocity of the stellar wind for each star. Another assumption we make is that the stellar wind velocity is terminal, but this velocity depends on the distance from the star as well.

We have not taken the hydrodynamic instabilities of the bow-shock structures into account. In comparison with the results of De Colle et al. [2014], we find that considering the hydrodynamic model of the evolution of the bow-shock structure does not lead to the same results and shapes we obtained. De Colle et al. [2014] shows the pericentre scenario in which, due to the rapid increase of the orbital star velocity, the ram pressures are unable to balance so the shock region

is much bigger and it definitely does not manifest itself with the symmetric shape of the shell in our models. This structure is broken because of the development of hydrodynamic instabilities (specifically Rayleigh-Taylor and Kelvin-Helmholtz instabilities) and strong tidal forces. But these hydrodynamic simulations were performed only for the the ambient medium at rest. Ballone et al. [2013] shows the hydrodynamic evolution of the stellar wind of the star that orbits the SMBH. At the sufficient distance from the SMBH, the stellar wind has mainly the radial symmetry. When it is much closer to the central SMBH, the radial symmetry breaks and the wind forms a thin layer along the axis of symmetry (we could hardly see our bow-shock shell with the cometary shape). Compared to our simplified results, the layer is not smooth as shown in our calculations but it has rather gaseous branched structure. On the other hand, the above mentioned hydrodynamic instabilities that destabilize the bow-shock structure can be inhibited by the magnetic field near the central black hole (this was not considered in works Ballone et al. [2013] and De Colle et al. [2014]). If the growth of hydrodynamic instabilities is suppressed by the magnetic field, then the bow shock shape and its evolution along the orbit should be comparable to our models.

Similar studies, which we were inspired by, were also performed in Zajaček et al. [2016]. This work includes an outflow scenario for the SMBH. The emission measure maps clearly show that the region around the apex of the bow-shock shell is the most luminous part of this structure. They calculated both thermal and non-thermal bow-shock emission for various outflow velocities. They opened up the possibility to study the outflow from the Galactic centre using stellar bow shocks, namely using the effect of orbital asymmetry of the bow-shock evolution. The outflow is a natural property of the radiatively inefficient accretion flows (RIAFs, see Yuan and Narayan [2014] for a review). To constrain the properties from observations, one needs precise timing and high-resolution observations of bow-shock sources near the Galactic centre, which is partially possible for objects in the S-cluster with 8-,10-meter class telescopes, but it will be even more interesting with interferometer GRAVITY and Extremely Large Telescope in the future.

From our proposed model in this thesis, where the bow-shock shell profile is seen from the inclination angle 90°, we are able to calculate the maximum observable value of the standoff distance for the changes of the bow-shock shell along the orbit.

If we used ESO VLT 8 m telescope, the angular resolution for Ks (2.2 μm) and L′ (3.8 μm) bands would be approximately $0.07''$ and $0.12''$, respectively. The changes of the standoff distance ΔR_0 for the fiducial S-star, one, two or ten years after the pericentre passage are shown in Tab. 4.1 (the values for the combined

	medium at rest	outflow	inflow
$\Delta R_0['']$ (after 1 year)	$1.1 \cdot 10^{-3}$	$1.6 \cdot 10^{-3}$	$7.9 \cdot 10^{-4}$
$\Delta R_0['']$ (after 2 years)	$2.1 \cdot 10^{-3}$	$3.4 \cdot 10^{-3}$	$1.4 \cdot 10^{-3}$
$\Delta R_0['']$ (after 10 years)	$7.7 \cdot 10^{-3}$	0.03	$4.1 \cdot 10^{-3}$

Table 4.1. Changes of the standoff distance ΔR_0 after the period of time (1, 2, 10 years) from the pericentre passage.

model are identical with the inflow model so we do not mention them in the table). Parameter ΔR_0 is computed as $\Delta R_0 = R_0(t) - R_0(t = 0)$, where t refers to time, $R_0(t)$ is the standoff distance in specific time after the pericentre passage (1, 2 or 10 years) and $R_0(t = 0)$ is the standoff distance at the pericentre. For the outflow and the inflow model, we consider V_0 to be 1000 km/s. We can conclude that these changes would not be observable with 8 m telescope in both previously mentioned bands.

On the other hand, if we used ESO E-ELT telescope, which is planned to have the diameter of the primary mirror 39 m, the angular resolution for Ks band should be approximately $0.014''$ and for L$'$ band it should be $0.024''$. This means that all of the changes from Tab. 4.1, except the case of the outflow model for the change after 10 years, would not be observed. However, the change ΔR_0 after 10 years for the outflow model would be observable in both Ks and L$'$ bands.

5. Conclusions and Future Prospects

The thesis is focused on the Galactic centre and the numerous coherent dusty and gaseous structures in its vicinity, especially bow shocks, which are observed not only in our cosmic neighbourhood, but they are common everywhere in Nature. The outline of the thesis and the history of the problem were described in Chapter 1 (Introduction).

In Chapter 2 we introduced the basic relations that we have employed from Wilkin [1996] for thin axisymmetric bow shocks that occur through the supersonic passage of the wind-blowing star with respect to its surrounding ambient medium. It was assumed that the internal momentum within the shell of the bow shock is conserved and the cooling process is so effective that the bow-shock shell has a negligible thickness in comparison with the distance to the star. Considering the balance of the ram pressures between the stellar wind and the ambient medium, we obtained an important parameter R_0, so-called standoff distance, which scales the size of the bow-shock shell. The bigger the value of R_0 is, the larger the shell becomes. Afterwards, we summarized Wilkin's exact analytic solutions for the shape of the bow shock, the tangential velocity in its shell and the mass surface density of the shell. Then we discussed the number density profile of the ambient medium considering the hydrostatical equilibrium near the Galactic centre. Compared to the observations of Wang et al. [2013] we inferred that this was not the probable scenario for the region near the SMBH.

The main results of this thesis can be found in Chapter 3. We presented four possible cases of a steady flow of an ambient medium for our fiducial S-star. We proved that the model for the zero velocity of the ambient medium behaves symmetrically with respect to the pericentre passage. On the other hand, the behaviour of other three models is asymmetric and they behave differently in the pre-pericentre phase compared to the post-pericentre phase.

The profile of the standoff distance for the outflow model is more asymmetric after the pericentre passage, while the standoff distance profile for the inflow model behaves more asymmetrically in the pre-pericentre phase. The combined model shows the most asymmetric behaviour. The profiles for the star velocity for all considered models show the same symmetries (or lack of them) as the profiles for the standoff distance during the pre-pericentre versus post-pericentre phase.

Then we discussed profiles of the tangential velocity in the shell and the mass surface density of the shell in different points along the fiducial S-star orbit. These profiles strongly depend on the ratio of the star velocity and its wind (parameter α), which varies along the orbit of the fiducial S-star. As the relative star velocity along the orbit changes for various models (ambient medium at rest/outflow/inflow/combined model), the profiles of these models are also different. The possibilities for different α are shown in Fig. 3.21.

Based on observations for the Bondi radius (see Wang et al. [2013]) of our Galaxy centre, we suggest that the inflow model is the most suitable model to describe the interaction with our fiducial S-star.

The above-mentioned results suggest new open question that should be addressed in the future. We would like to understand processes near the Galactic centre in deeper way and focus on less-simplified models of dusty and gaseous structures, namely, bow shocks. Our future work will comprehend 3D models of bow-shock shells with the consideration of their orientation, as defined by the inclination angle. Then it will be possible to obtain the luminosity profiles and compare them with data. We could upgrade our combined model and derive more realistic profiles without the artificial jumps at the Bondi radius. In this case we will use previously developed models for a self-consistent, stationary solution for the spherically symmetric accretion flows near the central supermassive black hole by Silich et al. [2008]. As long as we performed only calculations for thin axisymmetric bow shocks, we will generalise our models to the case of nonaxisymmetric bow shocks, for which exact analytic solutions are also known [Wilkin, 2000] (see for example Fig. 5.1).

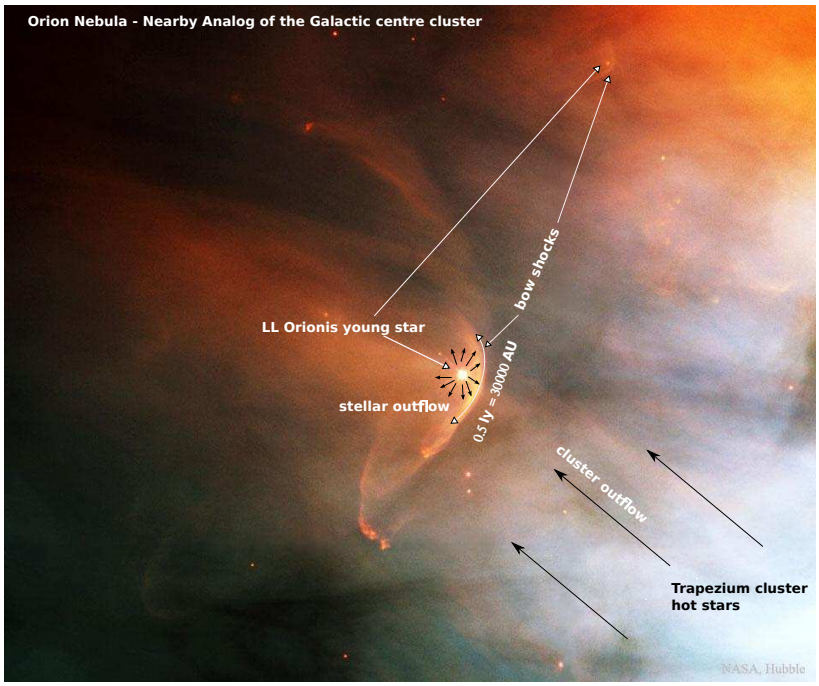

Figure 5.1. A bow shock is created by LL Orionis young star, as its wind collides with the surrounding interstellar medium of the Orion Nebula central star cluster (Trapezium region is seen in the lower-right corner). The bow-shock structure is about half a light year across. A non-symmetrical shape of this bow shock motivates us to study more complicated geometry of the bow-shock formation and evolution in the future work, where astrophysically realistic conditions will be taken into account (image credit: Hubble Heritage Team – AURA/STScI; C. R. O'Dell – Vanderbilt Univ; NASA).

As the astronomy itself is being advanced mainly by observations, and the theoretical models are often developed to describe and explain existing observational discoveries, one of our future prospects could be putting the emphasis on the observed data and their association with theoretical models. In order to initiate this research direction, we downloaded Ks band NACO data from ESO archive and made a picture that is shown in Fig. 5.2. It is obvious that this picture should be further analysed and all technical aspects, such as flat field, bias, dark current, hot pixels, etc., should be removed. We would like to progress in this field as well. For the moment we just marked the picture with the location

of Sgr A*, S-cluster and the main sources in the closest neighbourhood of the SMBH in the centre of our Galaxy.

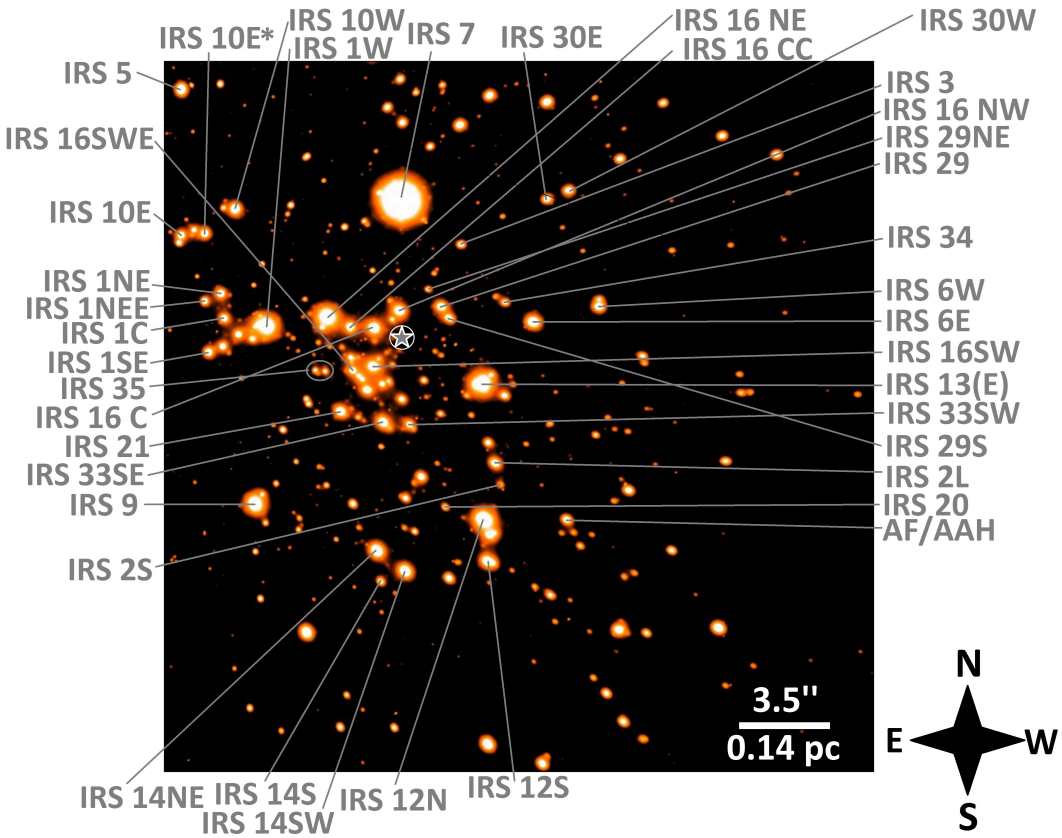

Figure 5.2. An infrared image of Sgr A* (grey star) and sources in its vicinity. A small white circle around Sgr A* represents the approximate location of S-cluster. Most of the labelled stars have been identified in Eckart et al. [2005] and Viehmann et al. [2005]. The image represents an area of approximately $(28 \times 28)''$ (1024×1024 pixels, the pixel scale is $0.027150''$ per pixel).

Bibliography

D. C. Backer and R. A. Sramek. Apparent proper motions of the galactic center compact radio source and PSR 1929+10. *ApJ*, 260:512–519, September 1982. doi: 10.1086/160273.

B. Balick and R. L. Brown. Intense sub-arcsecond structure in the galactic center. *ApJ*, 194:265–270, December 1974. doi: 10.1086/153242.

A. Ballone, M. Schartmann, A. Burkert, S. Gillessen, R. Genzel, T. K. Fritz, F. Eisenhauer, O. Pfuhl, and T. Ott. Hydrodynamical Simulations of a Compact Source Scenario for the Galactic Center Cloud G2. *ApJ*, 776:13, October 2013. doi: 10.1088/0004-637X/776/1/13.

V. B. Baranov, K. V. Krasnobaev, and A. G. Kulikovskii. A Model of the Interaction of the Solar Wind with the Interstellar Medium. *Soviet Physics Doklady*, 15:791, March 1971.

M. Bartusiak. *Black Hole: How an Idea Abandoned by Newtonians, Hated by Einstein, and Gambled On by Hawking Became Loved*. 2015.

E. E. Becklin and G. Neugebauer. Infrared Observations of the Galactic Center. *ApJ*, 151:145, January 1968. doi: 10.1086/149425.

E. E. Becklin, I. Gatley, and M. W. Werner. Far-infrared observations of Sagittarius A - The luminosity and dust density in the central parsec of the Galaxy. *ApJ*, 258:135–142, July 1982. doi: 10.1086/160060.

R. D. Blandford and M. C. Begelman. On the fate of gas accreting at a low rate on to a black hole. *MNRAS*, 303:L1–L5, February 1999. doi: 10.1046/j.1365-8711.1999.02358.x.

H. Bondi. On spherically symmetrical accretion. *MNRAS*, 112:195, 1952. doi: 10.1093/mnras/112.2.195.

A. E. Broderick and A. Loeb. Frequency-dependent Shift in the Image Centroid of the Black Hole at the Galactic Center as a Test of General Relativity. *ApJL*, 636:L109–L112, January 2006. doi: 10.1086/500008.

A. E. Broderick, V. L. Fish, S. S. Doeleman, and A. Loeb. Constraining the Structure of Sagittarius A*'s Accretion Flow with Millimeter Very Long Baseline Interferometry Closure Phases. *ApJ*, 738:38, September 2011. doi: 10.1088/0004-637X/738/1/38.

F. De Colle, A. C. Raga, F. F. Contreras-Torres, and J. C. Toledo-Roy. A Stellar Wind Origin for the G2 Cloud: Three-dimensional Numerical Simulations. *ApJL*, 789:L33, July 2014. doi: 10.1088/2041-8205/789/2/L33.

J. Dexter, E. Agol, P. C. Fragile, and J. C. McKinney. The Submillimeter Bump in Sgr A* from Relativistic MHD Simulations. *ApJ*, 717:1092–1104, July 2010. doi: 10.1088/0004-637X/717/2/1092.

A. Eckart and R. Genzel. Observations of stellar proper motions near the Galactic Centre. *Nature*, 383:415–417, October 1996. doi: 10.1038/383415a0.

A. Eckart, R. Schödel, and C. Straubmeier. *The black hole at the center of the Milky Way*. 2005.

A. Eckart, M. Horrobin, S. Britzen, M. Zamaninasab, K. Mužić, N. Sabha, B. Shahzamanian, S. Yazici, L. Moser, M. García-Marin, M. Valencia-S., A. Borkar, M. Bursa, G. Karssen, V. Karas, M. Zajaček, L. Bronfman, R. Finger, B. Jalali, M. Vitale, C. Rauch, D. Kunneriath, J. Moultaka, C. Straubmeier, Y. E. Rashed, K. Markakis, and A. Zensus. The infrared K-band identification of the DSO/G2 source from VLT and Keck data. In L. O. Sjouwerman, C. C. Lang, and J. Ott, editors, *The Galactic Center: Feeding and Feedback in a Normal Galactic Nucleus*, volume 303 of *IAU Symposium*, pages 269–273, May 2014. doi: 10.1017/S1743921314000726.

F. Eisenhauer, R. Genzel, T. Alexander, R. Abuter, T. Paumard, T. Ott, A. Gilbert, S. Gillessen, M. Horrobin, S. Trippe, H. Bonnet, C. Dumas, N. Hubin, A. Kaufer, M. Kissler-Patig, G. Monnet, S. Ströbele, T. Szeifert, A. Eckart, R. Schödel, and S. Zucker. SINFONI in the Galactic Center: Young Stars and Infrared Flares in the Central Light-Month. *ApJ*, 628:246–259, July 2005. doi: 10.1086/430667.

R. Genzel, C. Pichon, A. Eckart, O. E. Gerhard, and T. Ott. Stellar dynamics in the Galactic Centre: proper motions and anisotropy. *MNRAS*, 317:348–374, September 2000. doi: 10.1046/j.1365-8711.2000.03582.x.

A. M. Ghez, B. L. Klein, M. Morris, and E. E. Becklin. High Proper-Motion Stars in the Vicinity of Sagittarius A*: Evidence for a Supermassive Black Hole at the Center of Our Galaxy. *ApJ*, 509:678–686, December 1998. doi: 10.1086/306528.

A. M. Ghez, M. Morris, E. E. Becklin, A. Tanner, and T. Kremenek. The accelerations of stars orbiting the Milky Way's central black hole. *Nature*, 407: 349–351, September 2000. doi: 10.1038/407349a.

A. M. Ghez, G. Duchêne, K. Matthews, S. D. Hornstein, A. Tanner, J. Larkin, M. Morris, E. E. Becklin, S. Salim, T. Kremenek, D. Thompson, B. T. Soifer, G. Neugebauer, and I. McLean. The First Measurement of Spectral Lines in a Short-Period Star Bound to the Galaxy's Central Black Hole: A Paradox of Youth. *ApJL*, 586:L127–L131, April 2003. doi: 10.1086/374804.

A. M. Ghez, S. Salim, N. N. Weinberg, J. R. Lu, T. Do, J. K. Dunn, K. Matthews, M. R. Morris, S. Yelda, E. E. Becklin, T. Kremenek, M. Milosavljevic, and J. Naiman. Measuring Distance and Properties of the Milky Way's Central Supermassive Black Hole with Stellar Orbits. *ApJ*, 689:1044-1062, December 2008. doi: 10.1086/592738.

S. Gillessen, F. Eisenhauer, T. K. Fritz, H. Bartko, K. Dodds-Eden, O. Pfuhl, T. Ott, and R. Genzel. The Orbit of the Star S2 Around SGR A* from Very Large Telescope and Keck Data. *ApJL*, 707:L114–L117, December 2009. doi: 10.1088/0004-637X/707/2/L114.

S. Gillessen, R. Genzel, T. K. Fritz, F. Eisenhauer, O. Pfuhl, T. Ott, M. Schartmann, A. Ballone, and A. Burkert. Pericenter Passage of the Gas Cloud G2 in the Galactic Center. *ApJ*, 774:44, September 2013. doi: 10.1088/0004-637X/774/1/44.

L. Hanyk. Numerical recipes - Euler method. `http://geo.mff.cuni.cz/users/hanyk/NOFY056/2014/05-NR.pdf`, 2005. [Online; accessed 15-April-2016].

W. Herschel. On the Construction of the Heavens. *Philosophical Transactions of the Royal Society of London Series I*, 75:213–266, 1785.

I. Kant. *Allgemeine Naturgeschichte und Theorie des Himmels*. 1755.

J. C. Kapteyn. To what Stellar System does our Sun belong? (Abstract). *Publications of the ASP*, 4:259, November 1892. doi: 10.1086/120516.

D. Kunneriath, A. Eckart, S. N. Vogel, P. Teuben, K. Mužić, R. Schödel, M. García-Marín, J. Moultaka, J. Staguhn, C. Straubmeier, J. A. Zensus, M. Valencia-S., and V. Karas. The Galactic centre mini-spiral in the mm-regime. *A&A*, 538:A127, February 2012. doi: 10.1051/0004-6361/201117676.

C. C. Lang and M. R. Drout. The Galactic Center Magnetic Field on Smaller Scales: Multifrequency Observations of Nonthermal Filament Candidates. In M. R. Morris, Q. D. Wang, and F. Yuan, editors, *The Galactic Center: a Window to the Nuclear Environment of Disk Galaxies*, volume 439 of *Astronomical Society of the Pacific Conference Series*, page 53, May 2011.

C. C. Lang, W. M. Goss, C. Cyganowski, and K. I. Clubb. A High-resolution Survey of H I Absorption Toward the Central 200 pc of the Galactic Center. *ApJS*, 191:275–300, December 2010. doi: 10.1088/0067-0049/191/2/275.

C. C. Lang, J. Toomey, D. Ludovici, A. Mao, and M. Morris. The nature and origin of the Galactic center radio arc: a VLA Faraday study. In L. O. Sjouwerman, C. C. Lang, and J. Ott, editors, *The Galactic Center: Feeding and Feedback in a Normal Galactic Nucleus*, volume 303 of *IAU Symposium*, pages 461–463, May 2014. doi: 10.1017/S174392131400115X.

J. Langer and J. Podolský. Teoretická Mechanika. `http://utf.mff.cuni.cz/vyuka/OFY003/TEXTY/kontinuum.pdf`, 2013. [Online; accessed 19-April-2016].

H. S. Leavitt and E. C. Pickering. Periods of 25 Variable Stars in the Small Magellanic Cloud. *Harvard College Observatory Circular*, 173:1–3, March 1912.

Y. Levin and A. M. Beloborodov. Stellar Disk in the Galactic Center: A Remnant of a Dense Accretion Disk? *ApJL*, 590:L33–L36, June 2003. doi: 10.1086/376675.

B. Lindblad. The velocity ellipsoid, galactic rotation, and the dimensions of the stellar system. *MNRAS*, 90:503, March 1930. doi: 10.1093/mnras/90.5.503.

H. S. Liszt, J. M. van der Hulst, W. B. Burton, and M. P. Ondrechen. VLA synthesis of H I absorption toward SGR A. *A&A*, 126:341–351, October 1983.

B. Luzum, N. Capitaine, A. Fienga, W. Folkner, T. Fukushima, J. Hilton, C. Hohenkerk, G. Krasinsky, G. Petit, E. Pitjeva, M. Soffel, and P. Wallace. The IAU 2009 system of astronomical constants: the report of the IAU working group on numerical standards for Fundamental Astronomy. *Celestial Mechanics and Dynamical Astronomy*, 110:293–304, August 2011. doi: 10.1007/s10569-011-9352-4.

S. Markoff. The Role and Power of Jets Across the Black Hole Mass Scale. In *AAS/High Energy Astrophysics Division*, volume 13 of *AAS/High Energy Astrophysics Division*, page 205.04, April 2013a.

S. Markoff. Quasars in miniature: new insights into particle acceleration from X-ray binaries. In *APS April Meeting Abstracts*, April 2013b.

S. Markoff, M. A. Nowak, E. Gallo, R. Hynes, J. Wilms, R. M. Plotkin, D. Maitra, C. V. Silva, and S. Drappeau. As Above, So Below: Exploiting Mass Scaling in Black Hole Accretion to Break Degeneracies in Spectral Interpretation. *ApJL*, 812:L25, October 2015. doi: 10.1088/2041-8205/812/2/L25.

L. Meyer, A. M. Ghez, R. Schödel, S. Yelda, A. Boehle, J. R. Lu, T. Do, M. R. Morris, E. E. Becklin, and K. Matthews. The Shortest-Known-Period Star Orbiting Our Galaxys Supermassive Black Hole. *Science*, 338:84, October 2012. doi: 10.1126/science.1225506.

P. J. Mohr and B. N. Taylor. CODATA Recommended Values of the Fundamental Physical Constants: 1998. *Journal of Physical and Chemical Reference Data*, 28:1713–1852, November 1999. doi: 10.1063/1.556049.

K. Mužić, A. Eckart, R. Schödel, R. Buchholz, M. Zamaninasab, and G. Witzel. Comet-shaped sources at the Galactic center. Evidence of a wind from the central 0.2 pc. *A&A*, 521:A13, October 2010. doi: 10.1051/0004-6361/200913087.

J. Naiman, M. Soares-Furtado, and E. Ramirez-Ruiz. Modeling the Tenuous Intracluster Medium in Globular Clusters. *ArXiv e-prints*, October 2013.

J. H. Oort. Observational evidence confirming Lindblad's hypothesis of a rotation of the galactic system. *BAIN*, 3:275, April 1927a.

J. H. Oort. Investigations concerning the rotational motion of the galactic system together with new determinations of secular parallaxes, precession and motion of the equinox (Errata: 4 94). *BAIN*, 4:79, September 1927b.

J. H. Oort. Additional notes concerning the rotation of the galactic system. *BAIN*, 4:91, October 1927c.

J. H. Oort. The galactic nucleus. In H. van Woerden, R. J. Allen, and W. B. Burton, editors, *The Milky Way Galaxy*, volume 106 of *IAU Symposium*, pages 349–363, 1985.

J. H. Oort and L. Plaut. The distance to the galactic centre derived from RR Lyrae variables, the distribution of these variables in the galaxy's inner region and halo, and a rediscussion of the galactic rotation constants. *ApJ*, 41:71–86, June 1975.

J. H. Oort and G. W. Rougoor. The position of the galactic centre. *MNRAS*, 121:171, 1960. doi: 10.1093/mnras/121.2.171.

C. H. Payne. *Stellar Atmospheres; a Contribution to the Observational Study of High Temperature in the Reversing Layers of Stars.* PhD thesis, RADCLIFFE COLLEGE., 1925.

W.H. Press, S.A. Teukolsky, W.T. Vetterling, and B.P. Flannery. Numerical Recipes In C - The Art Of Scientific Computing. `http://www2.units.it/ipl/students_area/imm2/files/Numerical_Recipes.pdf`, 1998. [Online; accessed 15-April-2016].

J. Puls, J. S. Vink, and F. Najarro. Mass loss from hot massive stars. *A&A Rev.*, 16:209–325, December 2008. doi: 10.1007/s00159-008-0015-8.

C. Rauch, K. Mužić, A. Eckart, R. M. Buchholz, M. García-Marín, N. Sabha, C. Straubmeier, M. Valencia-S., and S. Yazici. A peek behind the dusty curtain: K_S-band polarization photometry and bow shock models of the Galactic center source IRS 8. *A&A*, 551:A35, March 2013. doi: 10.1051/0004-6361/201219874.

M. J. Reid, A. C. S. Readhead, R. C. Vermeulen, and R. N. Treuhaft. The Proper Motion of Sagittarius A*. I. First VLBA Results. *ApJ*, 524:816–823, October 1999. doi: 10.1086/307855.

G. H. Rieke and M. J. Lebofsky. Comparison of galactic center with other galaxies. In G. R. Riegler and R. D. Blandford, editors, *The Galactic Center*, volume 83 of *American Institute of Physics Conference Series*, pages 194–203, 1982. doi: 10.1063/1.33487.

J. Sanchez-Bermudez, R. Schödel, A. Alberdi, K. Muzić, C. A. Hummel, and J.-U. Pott. Properties of bow-shock sources at the Galactic center. *A&A*, 567: A21, July 2014. doi: 10.1051/0004-6361/201423657.

R. H. Sanders. The circumnuclear material in the Galactic Centre - A clue to the accretion process. *MNRAS*, 294:35, February 1998. doi: 10.1046/j.1365-8711.1998.01127.x.

R. H. Sanders. *Revealing the Heart of the Galaxy.* March 2014.

N. Scoville and A. Burkert. The Galactic Center Cloud G2—a Young Low-mass Star with a Stellar Wind. *ApJ*, 768:108, May 2013. doi: 10.1088/0004-637X/768/2/108.

H. Shapley. A Determination of the Distance to the Galactic Center. *Proceedings of the National Academy of Science*, 25:113–118, March 1939. doi: 10.1073/pnas.25.3.113.

S. Silich, G. Tenorio-Tagle, and F. Hueyotl-Zahuantitla. Spherically Symmetric Accretion onto a Black Hole at the Center of a Young Stellar Cluster. *ApJ*, 686:172-180, October 2008. doi: 10.1086/591226.

M. Tsuboi, Y. Kitamura, M. Miyoshi, K. Uehara, T. Tsutsumi, and A. Miyazaki. Galactic center mini-spiral by ALMA: Possible origin of the central cluster. *Publications of the ASJ*, April 2016. doi: 10.1093/pasj/psw031.

M. Valencia-S., A. Eckart, M. Zajaček, F. Peissker, M. Parsa, N. Grosso, E. Mossoux, D. Porquet, B. Jalali, V. Karas, S. Yazici, B. Shahzamanian, N. Sabha, R. Saalfeld, S. Smajic, R. Grellmann, L. Moser, M. Horrobin, A. Borkar, M. García-Marín, M. Dovčiak, D. Kunneriath, G. D. Karssen, M. Bursa, C. Straubmeier, and H. Bushouse. Monitoring the Dusty S-cluster Object (DSO/G2) on its Orbit toward the Galactic Center Black Hole. *ApJ*, 800:125, February 2015. doi: 10.1088/0004-637X/800/2/125.

T. Viehmann, A. Eckart, R. Schödel, J. Moultaka, C. Straubmeier, and J.-U. Pott. L- and M-band imaging observations of the Galactic Center region. *A&A*, 433: 117–125, April 2005. doi: 10.1051/0004-6361:20041748.

R. Voss, R. Diehl, D. H. Hartmann, M. Cerviño, J. S. Vink, G. Meynet, M. Limongi, and A. Chieffi. Using population synthesis of massive stars to study the interstellar medium near OB associations. *A&A*, 504:531–542, September 2009. doi: 10.1051/0004-6361/200912260.

Q. D. Wang, M. A. Nowak, S. B. Markoff, F. K. Baganoff, S. Nayakshin, F. Yuan, J. Cuadra, J. Davis, J. Dexter, A. C. Fabian, N. Grosso, D. Haggard, J. Houck, L. Ji, Z. Li, J. Neilsen, D. Porquet, F. Ripple, and R. V. Shcherbakov. Dissecting X-ray-Emitting Gas Around the Center of Our Galaxy. *Science*, 341: 981–983, August 2013. doi: 10.1126/science.1240755.

Francis P. Wilkin. Exact analytic solutions for stellar wind bow shocks. *ApJL*, 459(1):L31, 1996. URL `http://stacks.iop.org/1538-4357/459/i=1/a=L31`.

Francis P. Wilkin. Modeling nonaxisymmetric bow shocks: Solution method and exact analytic solutions. *ApJ*, 532(1):400, 2000. URL `http://stacks.iop.org/0004-637X/532/i=1/a=400`.

E. R. Wollman, T. R. Geballe, J. H. Lacy, C. H. Townes, and D. M. Rank. NE II 12.8 micron emission from the galactic center. II. *ApJL*, 218:L103–L107, December 1977. doi: 10.1086/182585.

T. Wright. *An original theory or new hypothesis of the universe : founded upon general phaenomena of the visible creation; and particularly the Via the laws of nature, and solving by mathematical principles : the Lactea ...compris'd in nine familiar letters from the author to his friendand : illustrated with upward of thirty graven and mezzotinto plates ...* 1750. doi: 10.3931/e-rara-28672.

F. Yuan and R. Narayan. Hot Accretion Flows Around Black Holes. *ARA&A*, 52:529–588, August 2014. doi: 10.1146/annurev-astro-082812-141003.

F. Yusef-Zadeh, M. Wardle, R. Schödel, D. A. Roberts, W. Cotton, H. Bushouse, R. Arendt, and M. Royster. Sgr A* and Its Environment: Low-mass Star Formation, the Origin of X-Ray Gas and Collimated Outflow. *ApJ*, 819:60, March 2016. doi: 10.3847/0004-637X/819/1/60.

M. Zajaček. Neutron stars near a galactic centre. *Master Thesis, Charles University in Prague, 150 pp. (2014)*, June 2014.

M. Zajaček, A. Eckart, F. Peissker, G. D. Karssen, and V. Karas. Infrared-excess Source DSO/G2 Near the Galactic Center: Theory vs. Observations. In *Proceedings of the 24th Annual Conference of Doctoral Students - WDS 2015 - Physics (eds. J. Safrankova and J. Pavlu), Prague, Matfyzpress, pp. 27-35, 2015; ISBN 978-80-7378-311-2*, pages 27–35, December 2015.

M. Zajaček, A. Eckart, V. Karas, D. Kunneriath, B. Shahzamanian, N. Sabha, K. Mužić, and M. Valencia-S. Effect of an isotropic outflow from the Galactic Centre on the bow-shock evolution along the orbit. *MNRAS*, 455:1257–1274, January 2016. doi: 10.1093/mnras/stv2357.

Q. Zhang and X. Zheng. The Role of Bow Shocks in Bipolar Molecular Outflows. *ApJ*, 474:719–723, January 1997.

Appendices

A Euler method and its application in this work

The main task of Euler method is to solve the system of R linear ordinary differential equations of first order,[1]

$$\frac{dy_r(x)}{dx} = f_r(x, y_1(x), ..., y_R(x)), \qquad r = 1, ..., R, \qquad \frac{d\boldsymbol{y}(x)}{dx} = \boldsymbol{f}(x, \boldsymbol{y}(x)) \ , \quad (1)$$

with an initial condition

$$y_r(x_0) = y_{0,r}, \qquad \boldsymbol{y}(x_0) = \boldsymbol{y}_0 \ , \quad (2)$$

where $y_i(x)$ or $\boldsymbol{y}(x)$ refer to functions we then integrate. The system of equations of higher degrees can be simplified to the system of first order equations. The Euler method can be formulated in two variants: the implicit method and the explicit one. Both Euler methods are based on Taylor series of zero and first order. Our brief exposition follows Hanyk [2005] in the form employed for our numerical computations.

For a specific index of the equation r and for Taylor series evaluated at the point x_n or x_{n+1}

$$y(x_n + h) \approx y(x_n) + hy'(x_n) \qquad or \qquad y(x_{n+1} - h) \approx y(x_{n+1}) - hy'(x_{n+1}) \ , \quad (3)$$

where h stands for the value for the size of each step. Associating eq. (1) and that $x_n + h := x_{n+1}$, $y(x_n) := y_n$, we get the formulations for one equation for explicit

$$y_{n+1} = y_n + hf(x_n, y_n), \qquad n = 0, 1, ... \ , \quad (4)$$

and implicit Euler method

$$y_{n+1} = y_n + hf(x_{n+1}, y_{n+1}), \qquad n = 0, 1, ... \ . \quad (5)$$

Considering the system of R eq. the explicit and implicit Euler methods are

$$y_{n+1,r} = y_{n,r} + hf(x_n, y_{n1}, ..., y_{nR}), \qquad \boldsymbol{y}_{n+1} = \boldsymbol{y}_n + h\boldsymbol{f}(x_n, \boldsymbol{y}_n) \ , \quad (6)$$

$$y_{n+1,r} = y_{n,r} + hf(x_{n+1}, y_{n+1,1}, ..., y_{n+1,R}), \qquad \boldsymbol{y}_{n+1} = \boldsymbol{y}_n + h\boldsymbol{f}(x_{n+1}, \boldsymbol{y}_{n+1}) \ , \quad (7)$$

respectively.

We need to mention that the Euler method is probably the least precise method from all the integration methods. It is only first-order method and the accuracy depends on the size of the step h. But on the other hand, for our research it is only essential to calculate the orbit of the star around the black hole. We only need one period and so this method is very appropriate. Furthermore, we can make the final results (e.g. positions or velocities) more accurate with shortening the step h, which corresponds to the time step dt in our program. The numerical accuracy of this method could manifest itself e.g. in the precession of the orbit. For more about the Euler method, see Hanyk [2005] and Press et al. [1998].

[1] *Leonhard Euler (1707-1783)*, a Swiss mathematician, logician, physicist, astronomer and engineer. In 1768, he published a textbook called *Institutionum calculi integralis* where, inter alia, a method was described for the numerical integration, nowadays known as *Euler method*.

As it was briefly said below, the program for computing positions and velocities in this work is based on Euler method. The basic script of it was written and provided by Michal Zajaček. Then we used the output of the integrator – calculated positions of a star and its orbital velocity along the orbit – for further calculations and analysis. The program itself consists of two parts, the main part for computing the orbit of the star around the SMBH and the second part is a subroutine for computing energy.

At the beginning we entry initial conditions for the position and the velocity of the star at the pericentre and specify the time of computing the orbit and the time step. We choose the size of the time step as $dt = 10^{-3}$. It is the N-body problem so we need to take the principle of the superposition into account, and then the Newton's second law is given by

$$m_i \boldsymbol{a_i} = \sum_{\substack{j=1 \\ j \neq i}}^{N} \boldsymbol{F}_j \qquad i = 1, ..., N \ , \tag{8}$$

where i refers to the body (with the mass m) that we are interested in. Whereas the bodies affect each other gravitationally, $\boldsymbol{F}$ is given by

$$\boldsymbol{F}_j = -G \sum_{\substack{j=1 \\ j \neq i}}^{N} \frac{m_i m_j}{|\boldsymbol{r}_i - \boldsymbol{r}_j|^2} \frac{\boldsymbol{r}_i - \boldsymbol{r}_j}{|\boldsymbol{r}_i - \boldsymbol{r}_j|} \ , \tag{9}$$

where G is a gravitational constant, m_i, m_j are the masses of the bodies and $\boldsymbol{r}_i, \boldsymbol{r}_j$ are position vectors of the bodies. The net acceleration is then derived from eq. (8) and eq. (9) as

$$\boldsymbol{a_i} = -G \sum_{\substack{j=1 \\ j \neq i}}^{N} \frac{m_j}{|\boldsymbol{r}_i - \boldsymbol{r}_j|^2} \frac{\boldsymbol{r}_i - \boldsymbol{r}_j}{|\boldsymbol{r}_i - \boldsymbol{r}_j|} \ . \tag{10}$$

After computing the accelerations we use the Euler method with the time step dt for computing new positions $\boldsymbol{r}$ and velocities $\boldsymbol{v}$ in each time t. Than the formulae are

$$\boldsymbol{v}_i(t + dt) = \boldsymbol{v}_i(t) + dt \cdot \boldsymbol{a}_i(t, \boldsymbol{v}_i(t)) \ , \tag{11}$$

$$\boldsymbol{r}_i(t + dt) = \boldsymbol{r}_i(t) + dt \cdot \boldsymbol{v}_i(t, \boldsymbol{r}_i(t)) \ . \tag{12}$$

We can identify these two equations with eq. (6) as:

$$\begin{aligned} \boldsymbol{y}_{n+1} &:= \boldsymbol{v}_i(t + dt), & \boldsymbol{y}_{n+1} &:= \boldsymbol{r}_i(t + dt) \ , \\ \boldsymbol{y}_n &:= \boldsymbol{v}_i(t), & \boldsymbol{y}_n &:= \boldsymbol{r}_i(t) \ , \\ \boldsymbol{f}(x_n, \boldsymbol{y}_n) &:= \boldsymbol{a}_i(t, \boldsymbol{v}_i(t)), & \boldsymbol{f}(x_n, \boldsymbol{y}_n) &:= \boldsymbol{v}_i(t, \boldsymbol{r}_i(t)) \ , \\ & & h &:= dt \ . \end{aligned}$$

In our case we restricted ourselves only two-body problem ($N = 2$) in the orbital plane, though, the method can handle multiple bodies.

The subroutine itself calculates the total energy in each time and allows us to compare it with the initial one. Afterwards, we are able to discuss the accuracy of this method. The difference between the new total energy and the initial energy in every step of all our simulations is less then 0,01 %.

B In honour of Ernst Mach

On 21st April 1887, Ernst Mach, together with his collaborator Peter Salcher, published a paper where he described in details the experiment with a supersonic bullet. This paper included the very first picture of the shock wave and also the description of the development of the detached front shock wave. He discussed the behaviour of the standoff distance with flight velocity and the bullet shape and he also pointed out that the same shock patterns might appear in astrophysics. The so-called Mach wave propagates from a supersonically moving point-like object. The wave is characterized by the Mach angle α – an angle of the front shock wave's asymptote:

$$\alpha = \arcsin\left(\frac{1}{M}\right) = \arcsin\left(\frac{a}{v}\right) \ , \tag{13}$$

where M is the Mach number, a is the speed of sound in the medium, and v is the velocity of local flow of the medium.

Figure 3. The memorial plate in honour of the eminent physicist Ernst Mach at Carolinum building of the Charles University in Prague.